Journal of Heat Transfer

# Technical Notes

This section contains shorter technical papers. These shorter papers will be subjected to the same review process as that for full papers.

## The Effect of Space-Dependent Thermal Conductivity on the Steady Central Temperature of a Cylinder

**Louis C. Burmeister**
e-mail: kume@mecheng.me.ukans.edu
Mem. ASME Department of Mechanical Engineering, University of Kansas, Lawrence, KS 66045

*A transformation is presented that enables the center temperature of a cylinder to be expressed in terms of an integral of the peripheral temperature distribution for heat conduction with space-dependent thermal conductivity. Its predictions agree with exact answers and with numerical solutions obtained with finite difference methods for four test cases. The new result can be applied to a two-dimensional floating random-walk Monte Carlo procedure which previously was restricted to the case of constant thermal conductivity.* [DOI: 10.1115/1.1418701]

*Keywords: Conduction, Cylinder, Heat Transfer, Monte Carlo, Space*

### Introduction

Accurate prediction of the temperature distribution in a solid requires solution of the heat diffusion equation. This can be done either with boundary conditions specified or to determine them from measured temperatures at internal locations, the latter as done by Ganesa-Pillai and Haji-Sheikh [1]. Complex geometries and boundary conditions often necessitate numerical methods of solution whether or not thermal conductivity is constant. The boundary element (Brebbia [2]) and floating random-walk Monte Carlo numerical methods (Haji-Sheikh and Sparrow [3]) are among those that utilize information obtained from exact relationships. For these methods to be accurate when thermal conductivity varies with position, it is desirable that relationships for that case be found.

The same mathematical problem is encountered in related areas. In Turner's [4,5] two-dimensional applications of Monte Carlo techniques to prediction of unsteady piezometric potential in a water well, it was observed that variation of hydraulic transmissibility with location ought to be taken into account.

While many analytical solutions are known if thermal conductivity $k$ is constant, few are known when it is space dependent. In their surveys of possibilities for that case, Bellman [6] and, especially, Luikov [7] point out that analytical solutions are generally possible only for restrictive cases, such as one-dimensional conductivity variation or conductivity constant in zones. For one-dimensional cases, transformation of the space coordinate $x$ as $\omega = \int dx/k(x)$ is a useful simplification. In physical terms, it gives the thermal resistance in the $x$ direction. Grigoriu [8] proposed a floating-random-walk Monte Carlo method based on properties of Brownian motion and Itô processes that is claimed to be applicable to space-dependent conductivity, but without examples.

Following a suggestion of Bellman [6], Munoz and Burmeister [9] utilized the substitution $y = k^{1/2}T$ to find that the steady heat diffusion equation is transformed into $\nabla^2 y = Fy$ in which $F = k^{-1/2}\nabla^2 k^{1/2}$. Then, analytical solutions can be obtained if $F$ is a convenient function. This substitution was advanced by Clements and Budhi [10] who incorporated a Kirchoff transformation (Carslaw and Jaeger [11]) to obtain a boundary element method for numerical solution of a class of problems in which thermal conductivity is dependent upon space and temperature. Munoz and Burmeister [9] explored the use of their results for a Monte Carlo numerical procedure. They found that when $F$ is a function of radius $r$ alone in cylindrical coordinates, the center temperature $T_c$ of a cylinder of radius $R$ is related to the peripheral temperature $T_R(\theta)$ and thermal conductivity $k_R(\theta)$ at angular location $\theta$ as

$$T_c = \int_0^{2\pi} T_R(\theta) k_R^{1/2}(\theta)\, d\theta / \overline{k_R^{1/2}} \quad \text{with} \quad \overline{k_R^{1/2}} = \int_0^{2\pi} k_R^{1/2}(\theta)\, d\theta / 2\pi \tag{1}$$

The relationship in Eq. (1) between the center and peripheral temperatures, although correct for the stated condition, lacks generality. For example, the common case of thermal conductivity varying stepwise as in a layered anisotropic material violates the condition that $F$ be continuous and depend only upon radius. In the following, another relationship will be derived and its predictions will be compared with those obtained by other means.

### Formulation

The steady heat diffusion equation in cylindrical coordinates is

$$\frac{1}{r}\frac{\partial\left(kr\dfrac{\partial T}{\partial r}\right)}{\partial r} + \frac{1}{r^2}\frac{\partial\left(k\dfrac{\partial T}{\partial \theta}\right)}{\partial \theta} = 0. \tag{2}$$

Integration of Eq. (2) with respect to $\theta$ from 0 to $2\pi$ gives

$$\frac{1}{r}\frac{\partial\left(\int_0^{2\pi} kr\dfrac{\partial T}{\partial r}\, d\theta\right)}{\partial r} + \frac{1}{r^2}\left[k(2\pi)\frac{\partial T(2\pi)}{\partial \theta} - k(0)\frac{\partial T(0)}{\partial \theta}\right] = 0.$$

Since conditions at the beginning and end of an angular traverse are the same, it follows that

$$\frac{d\left(\int_0^{2\pi} kr\dfrac{\partial T}{\partial r}\, d\theta\right)}{dr} = 0.$$

Contributed by the Heat Transfer Division for publication in the JOURNAL OF HEAT TRANSFER. Manuscript received by the Heat Transfer Division September 25, 2000; revision received July 10, 2001. Associate Editor: D. B. R. Kenning.

  

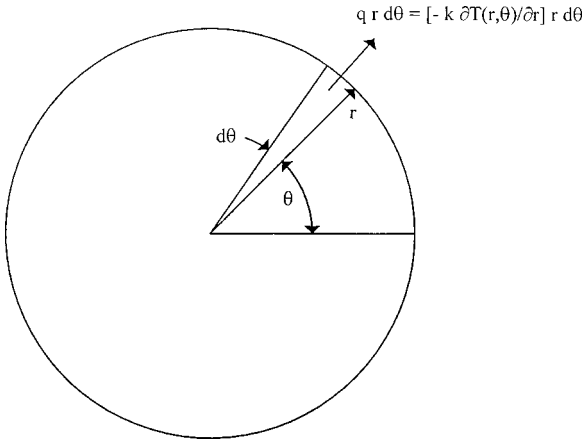


**Fig. 1 Conductive heat flux $q$ across a differential element of area $rd\theta$ on the periphery of a cylinder**

Integration with respect to $r$ from 0 to $r$ gives

$$\int_0^{2\pi} k(r,\theta) r \frac{\partial T(r,\theta)}{\partial r} d\theta = 0. \tag{3}$$

Equation (3) represents the physical requirement that the sum of steady heat flows into and out of a circle be zero as shown in Fig. 1, and the current development could have started with it.

Recasting Eq. (3) as

$$\int_0^{2\pi} \frac{1}{k^{-1}} \frac{\partial T(r,\theta)}{\partial r} d\theta = 0$$

motivates the coordinate transformations

$$\eta = \int_0^r \frac{dr'}{k(r',\theta)} \Bigg/ \int_0^R \frac{dr'}{k(r',\theta)} \tag{4}$$

and

$$f = \int_0^\theta \frac{d\theta'}{\int_0^R dr'/k(r',\theta')} \Bigg/ \int_0^{2\pi} \frac{d\theta}{\int_0^R dr'/k(r',\theta)}. \tag{5}$$

With the transformations of Eqs. (4) and (5), Eq. (3) becomes

$$\int_0^1 \frac{\partial T(\eta,f)}{\partial \eta} df = 0.$$

Integration with respect to $\eta$ from 0 to the outer radius of the cylinder gives the center temperature in terms of the specified peripheral temperature as

$$T_c = \int_0^1 T_R df. \tag{6}$$

## Discussion

The functional form of $f(\theta)$ in Eq. (5) is consistent with the previously cited observations by Bellman [6] and Luikov [7]. It is also consistent with the use by Hameed and Lebedeff [12] of the space variable transformation $\omega = \int dx/k(x)$ in an application of the integral method to heat conduction in media in which thermal conductivity varies one-dimensionally with position. Patankar's [13] use of the harmonic mean of thermal conductivity $k_{\text{eff}}$ between nodes in a finite difference numerical method as

$$2/k_{\text{eff},i} = 1/k_{i+1/2} + 1/k_{i-1/2}$$

is similar. Further support for the functional form of $f(\theta)$ is obtained from a finite difference formulation to determine the center temperature of a cylinder of specified peripheral temperature as depicted in Fig. 2. Use of only three control volumes around the central control volume for simplicity yields

$$T_c \left( \frac{1}{\frac{r_1}{k_o} + \frac{R-r_1}{k_{R1}}} + \frac{1}{\frac{r_1}{k_o} + \frac{R-r_1}{k_{R2}}} + \frac{1}{\frac{r_1}{k_o} + \frac{R-r_1}{k_{R3}}} \right) = \frac{T_{R1}}{\frac{r_1}{k_o} + \frac{R-r_1}{k_{R1}}} + \frac{T_{R2}}{\frac{r_1}{k_o} + \frac{R-r_1}{k_{R2}}} + \frac{T_{R3}}{\frac{r_1}{k_o} + \frac{R-r_1}{k_{R3}}}.$$

This finite difference expression suggests the continuous equivalent

$$T_c \int_0^{2\pi} \frac{1}{\int_0^R \frac{dr'}{k(r',\theta)}} d\theta = \int_0^{2\pi} T_R(\theta) \frac{1}{\int_0^R \frac{dr'}{k(r',\theta)}} d\theta,$$

which is consistent with Eq. (6). If interior control volumes are used between the central and the peripheral control volumes, a similar but more complex expression is obtained that contains additional, small terms that represent heat flow in the angular direction.

The first demonstration of the predictive ability of the formulation in Eq. (6) is for the one-dimensional case of a slab of two layers, each of thickness $L$. The temperature distribution is given by

$$\frac{d\left(k \frac{dT}{dx}\right)}{dx} = 0, \quad T(-L) = T_H, \quad T(L) = T_L,$$

$$k = \begin{cases} k_o(1+a), & x < 0 \\ k_o & \text{otherwise} \end{cases}.$$

The solution is

$$T = \begin{cases} T_H - (T_H - T_L)(x/L+1)/(2+a), & x < 0 \\ T_L - (T_H - T_L)(x/L-1)(1+a)/(2+a) & \text{otherwise} \end{cases}. \tag{7a}$$

The temperature $T_c$ at $x = 0$, the interface between the two layers, is

$$T_c = [(1+a)T_H + T_L]/(2+a). \tag{7b}$$

To compare the prediction of Eq. (6), it is first recognized that $x = r\cos(\theta)$ for a cylindrical coordinate system centered at $x = 0$. Then, the peripheral temperature at a constant radial distance, equal to the layer thickness, from the interface between the two layers is obtained from Eq. (7$a$) to be

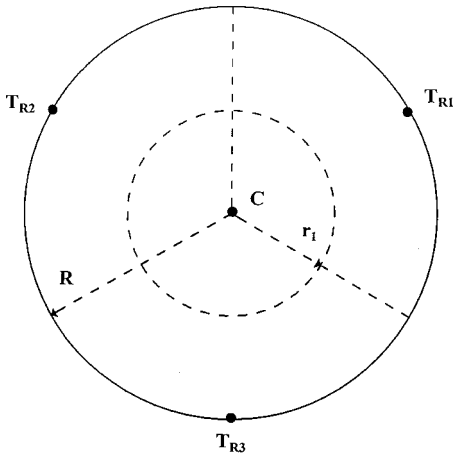


**Fig. 2 Control volumes for determination of the central temperature of a cylinder in terms of the peripheral temperatures by a finite difference method**

$$T_R=\begin{cases} T_H-(T_H-T_L)[1+\cos(\theta)]/(2+a), & \pi/2<\theta<3\pi/2 \\ T_L-(T_H-T_L)(1+a)[\cos(\theta)-1]/(2+a) & \text{otherwise} \end{cases}. \quad (8)$$

For this problem, Eq. (5) gives

$$f=\begin{cases} \theta/[(2+a)\pi], & 0\leqslant\theta<\pi/2 \\ [(1+a)\theta-a\pi/2]/[(2+a)\pi], & \pi/2\leqslant\theta<3\pi/2. \\ (\theta+a\pi)/[(2+a)\pi], & 3\pi/2\leqslant\theta<2\pi \end{cases} \quad (9)$$

Use of Eqs. (8) and (9) in Eq. (5) gives

$$T_c=\int_0^{2\pi} T_R(\theta)\frac{1}{\pi(2+a)}\begin{Bmatrix} 1, & -\pi/2\leqslant\theta<\pi/2 \\ 1+a, & \pi/2\leqslant\theta<3\pi/2 \end{Bmatrix} d\theta$$

$$=[(1+a)T_H+T_L]/(2+a),$$

which is identical to the exact answer in Eq. (7*b*). The earlier prediction of Eq. (1) is erroneous for this case in which $F$ is not solely a function of radius.

The second case is one for which Eq. (1) is exact. In this case the thermal conductivity variation is $k=[2+(r/R)\cos\theta]^2$, for which $F=0$. Application of Eq. (5) results in $f=(2\theta+\sin\theta)/4\pi$ which, when used in Eq. (6) with $T_R(\theta)=100(2+\cos\theta)$, yields

$$T_c=\frac{25}{\pi}\int_0^{2\pi}[4+4\cos(\theta)+\cos^2(\theta)]d\theta=225.$$

Munoz and Burmeister demonstrated by comparison with a finite difference numerical solution that this is the correct value for the center temperature.

A third case for which $F$ is not solely a function of radius has the thermal conductivity uniform in each of two zones as described by

$$k=\begin{cases} 1, & 0.3\leqslant r<0.5, \quad 0\leqslant\theta\leqslant\pi \\ 5 & \text{otherwise} \end{cases}$$

for which Eq. (6) gives

$$f=\begin{cases} 5\theta/14\pi, & 0\leqslant\theta\leqslant\pi \\ 5/14+9(\theta/\pi-1)/14 & \text{otherwise} \end{cases}.$$

With $T_R=100(2+\cos\theta)$ Eq. (6) then gives the center temperature as 200, agreeing exactly with the value obtained with a finite difference numerical method by Munoz [14].

## Use in a Monte Carlo Procedure

The result of the present analysis is Eq. (6) which can be recast into the form

$$T_c=\int_0^{2\pi} T_R(\theta)[df/d\theta]d\theta. \quad (10)$$

In this form it can be seen that $T_c$ is the expected value of a series of experiments for which the probability distribution function for an outcome $T_R(\theta)$ within the range $0\leqslant\theta\leqslant2\pi$ is $df/d\theta$. From this it follows that the cumulative distribution function is $f(\theta)$.

Equation (10) can be used in a two-dimensional floating random-walk Monte Carlo procedure.

In general, because the thermal conductivity dependence upon location would not be convenient, evaluation of the cumulative distribution function $f$ in Eq. (5) would have to be accomplished numerically.

## Conclusion

A transformation has been found that enables the center temperature of a cylinder to be expressed in terms of an integral of the peripheral temperature distribution for heat conduction with space-dependent thermal conductivity. The predictions of the new result agree with exact answers and with numerical solutions obtained with finite difference methods for four test cases. The new result can be applied to a two-dimensional floating random-walk Monte Carlo procedure which previously was restricted to the case of constant thermal conductivity.

## Nomenclature

$a$ = constant for conductivity variation, see Eq. (7)
$f$ = transformed angular coordinate, see Eq. (5)
$F$ = conductivity function
$k$ = thermal conductivity
$\overline{k_R}$ = thermal conductivity at radius $R$ averaged over a circle
$L$ = slab thickness
$q$ = radial conductive heat flux, $q=-k\partial T/\partial r$
$r'$ = dummy radial coordinate and position
$r$ = radial coordinate and position
$R$ = cylinder radius
$T$ = temperature
$x$ = space coordinate and position

### Greek Symbols

$\eta$ = transformed space coordinate, see Eq. (4)
$\theta$ = angular coordinate and position
$\pi$ = natural number, $\pi=3.1415\ldots$
$\omega$ = transformed space coordinate

### Subscripts

$c$ = at the center
eff = effective value
$H$ = high
$i$ = index
$L$ = low
$o$ = at the center
$R$ = at radial distance $R$

## References


[1] Ganesa-Pillai, M., and Haji-Sheikh, A., 1998, "A Critical Evaluation Of the Monte Carlo Method For Application To The Inverse Heat Conduction Problem," *Proc. ASME. Heat Transfer Div.-1998, Intl. Mech. Engr. Congr. And Exp*, Nov. 15–20, HTD-V. 361-5, pp. 95–107.

[2] Brebbia, C., 1984, *The Boundary Element Method For Engineers*, Pentech Press Ltd., Estover Road, Plymouth, Devon PL6 7PZ, Great Britain.

[3] Haji-Sheik, A., and Sparrow, E., 1967, "The Solution Of Heat Transfer Problems by Probability Methods," ASME J. Heat Transfer, **89**, pp. 121–131.

[4] Turner, J., 1978, "An Improved Monte Carlo Procedure For The Solution Of The Steady-State, Two-Dimensional Diffusion Equation With Application To Flow Through Porous Media," M. S. thesis, University of Kansas, Lawrence, KS.

[5] Turner, J., 1982, "Improved Monte Carlo Procedures For The Unsteady-State Diffusion Equation Applied To Water Well Fields," Ph. D. thesis, University of Kansas, Lawrence, KS.

[6] Bellman, R., 1952, *Stability Theory Of Differential Equations*, McGraw-Hill, p. 109.

[7] Luikov, A., 1971, "Methods Of Solving The Nonlinear Equations Of Unsteady-State Heat Conduction," Heat Transfer-Sov. Res., **3**, pp. 1–51.

[8] Grigoriu, M., 2000, "A Monte Carlo Solution Of Heat Conduction And Poisson Equations," ASME J. Heat Transfer, **122**, pp. 40–45.

[9] Munoz, A., and Burmeister, L., 1988, "Steady Conduction With Space-Dependent Conductivity," ASME J. Heat Transfer, **110**, pp. 778–780.

[10] Clements, D., and Budhi, W., 1999, "A Boundary Element Method For The Solution of a Class of Steady-State Problems for Anisotropic Media," ASME J. Heat Transfer, **121**, pp. 462–465.

[11] Carslaw, H., and Jaeger, J., 1959, *Conduction Of Heat In Solids*, Oxford University Press, p. 89.

[12] Hameed, S., and Lebedeff, S., 1975, "Application Of Integral Method To Heat Conduction In Nonhomogeneous Media," ASME J. Heat Transfer, **97**, pp. 304–305.

[13] Patankar, S., 1978, "A Numerical Method For Conduction In Composite Materials, Flow in Irregular Geometries and Conjugate Heat Transfer," *Proc. Sixth Int. Heat Transfer Conf.*, Toronto, Canada, Vol. 3, Paper No. CO-14, pp. 297–302.

[14] Munoz, A., 1984, "Variable Thermal Conductivity And The Monte Carlo Floating Random Walk," Master of Science thesis, University of Kansas, Lawrence, KS.

# Effective Radiative Properties of a Cylinder Array

**Chongshan Zhang**

**Abraham Kribus**
e-mail: avi.kribus@weizmann.ac.il

Environmental Sciences and Energy Research Dept.,
Weizmann Institute of Science,
Rehovot 76100, Israel

**Rami Ben-Zvi**
Solar Facilities Unit, Weizmann Institute of Science,
Rehovot 76100, Israel

*Fully anisotropic problems are found where the radiative interaction is due to small-scale elements that lack spherical symmetry, for example: fibrous insulation, finned heat sinks, plant canopies, and some solar energy absorbers. We present the effective bulk optical properties of a PM composed of small-scale opaque cylinders. The properties are derived from data generated by detailed Monte-Carlo numerical experiments. The data reduction procedure is relatively simple and does not require a full solution and optimization of the Radiative Transfer Equation. Benchmark cases are presented, comparing an exact solution (with geometric detail of the cylinder array) and an approximate solution using a continuous PM model with the effective volumetric properties.*
[DOI: 10.1115/1.1423317]

*Keywords: Cylinder, Heat Transfer, Modeling, Numerical Methods, Properties, Radiation*

## 1 Introduction

Treatment of radiative transport in Participating Media (PM) is usually limited to semianisotropic media, i.e., volumetric absorption and scattering coefficients that are independent of direction, and a degenerate scattering phase function depending only on the angle between the incident and outgoing radiation. In a fully anisotropic medium, the volumetric absorption and scattering coefficients depend on the direction of incident radiation, and the scattering phase function depends separately on both the incident and outgoing directions. A fully anisotropic PM can be a useful model in problems of radiation transport through media containing small-scale interacting elements that lack spherical symmetry and are not randomly oriented, for example fibrous insulation [1], finned heat sinks [2], plant canopies [3], and solar absorbers [4,5].

Producing a useful PM model of such a system requires finding the bulk optical properties of the equivalent PM. The optical properties often cannot be predicted from first principles and need to be derived from experimental data. A sample of the medium is exposed to a known incident radiation, and outgoing radiation fluxes in several directions are measured. To analyze the results, a guess for the optical properties is provided; the direct problem is solved by some approximation of the Radiative Transfer Equation (RTE); and the outgoing flux results are compared to the experimental measurement. The optical properties are then adjusted and the computation is repeated within an optimization process, until reasonable agreement is reached [6]. This can be a resource-consuming process due to the need to solve the RTE repeatedly.

Fully anisotropic media require a large number of parameters to describe the optical properties, and a large optimization problem with an embedded RTE solver may become prohibitively expensive. In a recent contribution [7] we have proposed an alternative method requiring only the direct solution of algebraic equations. In the current paper, this procedure is applied to a specific example of a complex medium modeled as an anisotropic PM. The model problem is a volume containing a regular array of cylinders [2,3,5]. The anisotropy is due to the difference between the direction along the cylinders and the directions in the plane perpendicular to the cylinders. The effective optical properties of this medium were derived from the results of a numerical experiment. The effective properties were then used to simulate a benchmark problem, and the results were compared to a reference solution.

## 2 Numerical Experiment

The sample was a cube containing a section of the cylinder array (Fig. 1). The array pitch is three cylinder diameters in both directions. The cylinders can be black, ideal diffuse reflectors, or gray absorbing (surface absorptivity 0.4) and diffusely reflecting.

The approach is based on the division of directional space into discrete solid angle intervals, following the Finite Volume method [8,9]. For convenience, we refer to these solid angle intervals as ordinates (although they are not identical to the classical definition from the Discrete Ordinate Method). Each of the optical properties has a distinct value within each ordinate, so that the number of unknowns is related to the number of ordinate directions chosen. The polar and azimuthal angles were divided into equal intervals. The directional grid resolution varied between $4\times4$ and $16\times8$ (16 division in $\phi$, 8, in $\theta$). The experiments were performed numerically, using a Monte Carlo ray tracing procedure. Simulated incident light was introduced within a single ordinate direction, and outgoing radiation was measured for each outgoing ordinate. The procedure was repeated with the incident light coming within other ordinates.

The analysis method of the experimental results was presented in detail in [7]. The general Finite Volume formulation of Fiterman et al. [10] was used, producing a coupled set of ordinary differential equations. The discrete RTE was integrated over the volume of the sample to produce integral energy balance equations. This volume averaging required several simplifying assumptions as described in [7]. The transmitted and the scattered contributions to the outgoing radiation were separated, and the extinction coefficient for each ordinate direction was found from an approximate equation involving only the transmitted contribu-

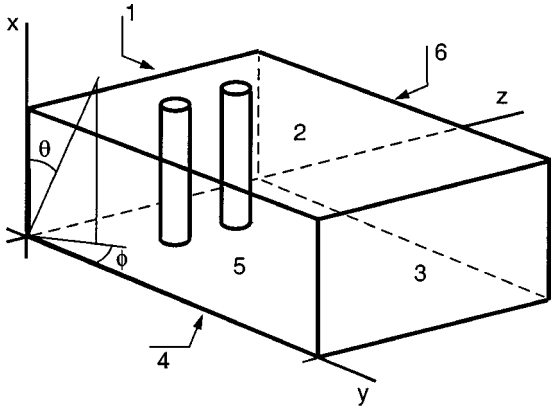


**Fig. 1 Geometry of the cylinder array**

Contributed by the Heat Transfer Division for publication in the JOURNAL OF HEAT TRANSFER. Manuscript received by the Heat Transfer Division September 1, 2000; revision received August 20, 2001. Associate Editor: D. A. Kaminski.

  

tion. The phase function was eliminated next by summing equations for all outgoing directions and using the energy conservation property of the phase function. This elimination produced equations for the scattering coefficient in each of the ordinate directions. Finally, given the extinction and scattering coefficients, a set of equations for the phase function can be solved. This procedure required solution of sets of algebraic equations, without the need for sophisticated solution methods of the RTE, and without iterative optimization.

## 3 Properties of the Cylinder Array

Figure 2 shows the distribution of the extinction coefficient of the array for a coarse and a fine directional grid. Each rectangle corresponds to the solid angle range of an ordinate. The extinction is low in directions along the cylinders' axis (small and large polar angle $\theta$), and high in directions perpendicular to the axis (intermediate $\theta$). The variations with the azimuthal angle $\phi$, visible in the high-resolution solution, correspond to the angles where the cylinders are aligned (minimal extinction) and staggered (maximum extinction). Each ordinate in the coarse grid solution is close to the average of the corresponding ordinates in the fine grid solution, with an average error of 0.5 percent. The optical properties at different resolutions are then consistent. The distribution of the scattering coefficient is similar to that of the extinction coefficient. The scattering albedo (ratio of scattering coefficient to extinction coefficient) is nearly constant over all ordinates, with an average value of 0.63, which is very close to the real surface reflectivity of 0.6.

Figure 3 presents selected distributions of the phase function. High phase function values are found in the azimuthal direction opposite to the incident direction, representing strong backward scattering. There is no "memory," however, of the incident polar angle since reflection from the cylinders is diffuse. Therefore, the medium is not truly backward scattering and cannot be modeled as a semi-anisotropic medium. The minima of the phase function are negative. This is clearly unphysical, and can be an artifact of the simplifications made in order to model the average scattered flux [7].

The statistical error of the Monte Carlo process is the analog of measurement errors in a physical experiment. The number of rays was changed between $10^4$ and $10^6$ for the case of 16 ordinates ($4\times4$). The largest error in the optical properties with $10^4$ rays was 4 percent. $10^5$ rays were used in the results presented here, with errors of at most 1 percent.

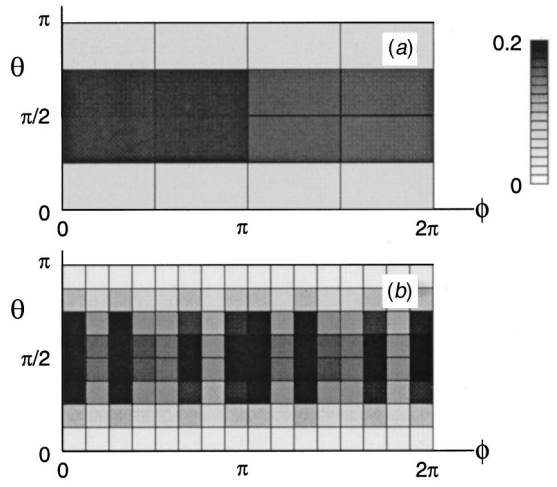


**Fig. 2 Anisotropic extinction coefficient as a function of polar and azimuthal angles: (*a*) ordinate resolution 4×4 and (*b*) ordinate resolution 16×8.**

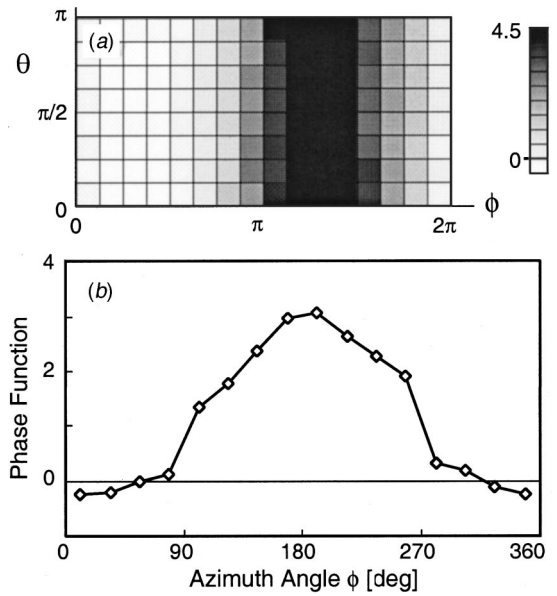


**Fig. 3 (*a*) Phase function of incident ordinates $3\pi/8<\theta<\pi/2$, $\pi/4<\phi<3\pi/8$, ordinate resolution 16×8; and (*b*) cross-section in the outgoing direction $3\pi/8<\theta<\pi/2$.**

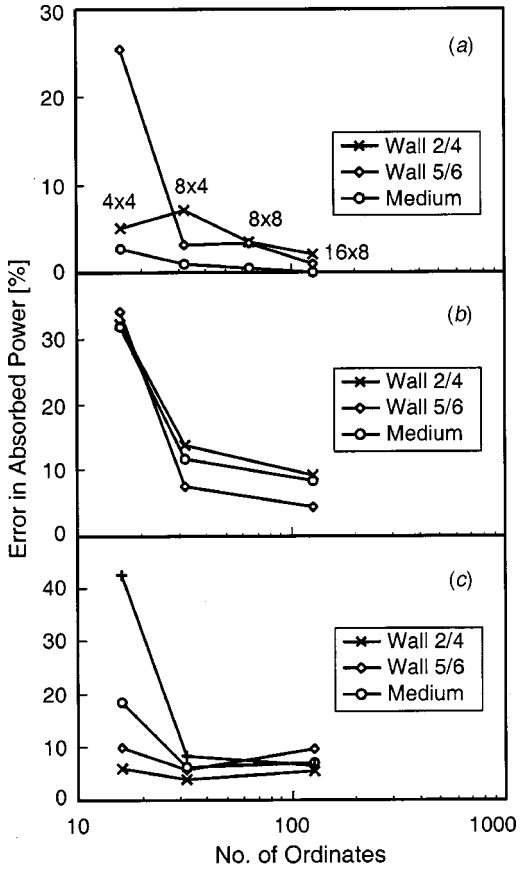


**Fig. 4 Benchmark results: convergence of errors in absorbed power with number of ordinates, for (*a*) absorbing cylinders, (*b*) reflecting cylinders (scattering medium), and (*c*) absorbing and reflecting cylinders**

The effective optical properties should be independent of the size of the sample if the PM model is valid. The size of the sample was increased by changing the number of cylinder rows between 3 and 6. The optical properties showed very little variation, indicating that even three rows produce a good representation of the behavior of the entire medium.

## 4 Benchmark Results and Discussion

The benchmark case is defined as a cubic box containing twelve rows of cylinders for an overall size of 36 diameters. Wall 1 of the cube at $y=0$ (Fig. 1) is hot, while all other walls and the cylinders are cold. All walls are black. We measure the distribution of the radiation emitted from wall 1 that is absorbed in the other walls and in the cylinders (i.e., the medium filling the box). The top and bottom (walls 2 and 4) are symmetric and are counted together. The sidewalls 5 and 6 are also symmetric. A reference solution was computed by detailed ray tracing of the full geometry of the cylinder array. The PM model results were computed by defining a continuous PM in the same volume as the cylinder array, using the effective optical properties that were presented in the previous section, and then performing ray tracing through the effective continuous medium.

Figure 4 shows the results for three cases: black cylinders (absorbing medium), reflective cylinders (scattering medium), and cylinders that are both absorbing and reflecting. The error is defined as the difference between the approximate solution (PM model using the effective properties) and the reference solution. The errors show convergence as a function of the number of ordinates in all three cases. Convergence is best for the absorbing case, but not as good for the two cases with a scattering component. Nevertheless, the errors for a $16\times 8$ directional resolution were less than 10 percent even in the presence of scattering, indicating that the solutions are useable even though not very accurate.

The representation of scattering seems to cause larger errors, as well as some negative values of the phase function. This is probably due to the simplifying assumptions that were used in the derivation of the scattering coefficients and the phase function [7]. Additional work is needed on improving the procedure for deriving the scattering properties. Nevertheless, as a first attempt to solve a complex problem that was not previously treated, the present results are a reasonable approximation.

## References


[1] Lee, S. C., 1990, ''Scattering Phase Function for Fibrous Media,'' Int. J. Heat Mass Transf., **33**, pp. 2183–2190.

[2] Sparrow, E. M., and Vemuri, S. B., 1985, ''Natural Convection/Radiation Heat Transfer From Highly Populated Pin-Fin Arrays,'' Journal of Heat Transfer, **107**, pp. 190–197.

[3] Mann, J., Curry, G., Demichele, D., and Baker, D., 1980, ''Light Penetration in a Row Crop With Random Plant Spacing,'' Agron. J., **72**, pp. 131–142.

[4] Thynell, S. T., and Merkle, C. L., 1989, ''Analysis of Volumetric Absorption of Solar Energy and Its Interaction With Convection,'' Journal of Heat Transfer, **111**, pp. 1006–1014.

[5] Karni, J., Kribus, A., Rubin, R., and Doron, P., 1998, ''The *Porcupine*: A Novel High-Flux Absorber for Volumetric Solar Receivers,'' ASME J. Sol. Energy Eng., **120**, pp. 85–95.

[6] Özisik, M. N., and Bokar, J. C., 1995, ''Inverse Problems of Radiative Transfer in Absorbing, Emitting and Scattering Media,'' *1st Int. Symp. Radiative Transfer*, M. P. Menguc, ed., Kusadasi, Turkey, Begell House, pp. 507–520.

[7] Zhang, C., Kribus, A., and Ben-Zvi, R., 2001, ''Volumetric Optical Properties of Fully Anisotropic Participating Media,'' J. Quant. Spectrosc. Radiat. Transf., **69**, pp. 27–42.

[8] Chui, E. H., and Raithby, G. D., 1993, ''Computation of Radiant Heat Transfer on a Nonorthogonal Mesh Using the Finite-Volume Method,'' Numer. Heat Transfer, Part B, **23**, pp. 269–288.

[9] Chai, J. C., Lee, H. S., and Patankar, S. V., 1994, ''Finite-Volume Method for Radiation Heat Transfer,'' J. Thermophys. Heat Transfer, **8**, pp. 419–425.

[10] Fiterman, A., Ben-Zvi, R., and Kribus, A., 1999, ''DOTS: Pseudo-Time-Stepping Solution of the Discrete-Ordinate Equations,'' Numer. Heat Transfer, Part B, **35**, pp. 163–183.


# Viscous Dissipation in Finite Thin-Gap Couette Devices


**Michael C. Wendl**
Research Associate and Affiliate Professor, School of Medicine and Department of Mechanical Engineering, Washington University, 4444 Forest Park Blvd., Box 8501, Saint Louis, MO 63108
e-mail: mwendl@watson.wustl.edu

**Ramesh K. Agarwal**
The William Palm Professor, Department of Mechanical Engineering, Washington University, 1 Brookings Drive, Box 1185, Saint Louis, MO 63130



*An analytical solution is reported for the temperature distribution in finite span thin-gap Couette devices which accounts for viscous dissipation. Taken in conjunction with an established solution for the stable velocity profile, this result describes the standard experimental configuration where no external heat fluxes are applied. We discuss physical aspects as well as conditions for which classical one-dimensional theory should be replaced by the present result.* [DOI: 10.1115/1.1418373]



*Keywords: Analytical, Conduction, Flow, Heat Transfer, Laminar*


## 1 Introduction

Couette flow devices [1] utilize the concept of two coaxial cylinders enclosing a working fluid. Motion is sustained via shear forces generated by rotating one of the cylinders. In ''thin-gap'' configurations, the ratio of gap size to inner cylinder radius is vanishingly small and fluid response is independent of which cylinder functions as the rotor. The basic design has been used in many practical applications, including viscometry [2] and fluid processing [3]. Moreover, it has evolved as a standard platform for studying fundamental phenomena, such as laminar transition [4–6] and viscous heating [7–10].

Couette devices are typically modeled using an idealized geometry where cylinder spans are considered infinite [4–11]. Spanwise effects imparted on the ends are neglected and the task of determining stable base flow and temperature distributions, i.e., the Couette problem, is reduced to one dimension. Here, velocity profiles assume the classical linear ''constant shear'' form and temperature profiles are parabolic if viscous heating is considered [11]. This treatment represents a significant theoretical simplification. Yet it is well-known that spanwise effects are appreciable in devices having small to moderate cylinder spans. This has been shown by numerous experimental investigations using aspect ratios on the order of 10 or less [12–14]. Thus, there exists a class of instruments for which idealized theory is clearly not sufficient [2,12].

An analytical solution for the Couette velocity profile in thin-gap devices having finite aspect ratios has long been available [15]. In the absence of viscous dissipation, the thermal problem is trivial since temperature can be inferred directly from the velocity profile. However, for non-trivial dissipation, e.g., Brinkman numbers in the $10^{-1}$ to $10^{2}$ range [7], heat generation terms in the temperature equation prevent leveraging the existing model. We


Contributed by the Heat Transfer Division for publication in the JOURNAL OF HEAT TRANSFER. Manuscript received by the Heat Transfer Division, July 27, 2000; revision received June 25, 2001. Associate Editor: J. Georgiadis.

present here an analytical solution for this case. In light of previous studies of viscous dissipation [7–10], we consider the implementation in which there are no externally applied heat fluxes.

## 2 Problem Formulation

Let gap size and total span be $H$ and $L$, respectively (where $L$ is finite). Also, define the translation velocity of the inner cylinder surface as $u_w$ and take $T_w$ to be a reference temperature. Fluid properties are constant density $\rho$, kinematic viscosity $\nu$, and thermal conductivity $k$. Pertinent non-dimensional parameters are the aspect ratio $\phi = L/H$ and the Brinkman number $\mathrm{Br} = [(\rho \nu u_w^2)/(kT_w)]$. The Reynolds number is relevant only to the extent that it is below a critical value for the onset of flow instability, a prerequisite for the existence of stable Couette flow. The seven parameter dimensional system therefore reduces to a two parameter dimensionless one defined by parameter space $(\mathrm{Br}, \phi)$. The parallel Couette flow model applied to the Navier-Stokes equations yields [16]

$$\nabla^2 u = 0, \tag{1}$$

and

$$\nabla^2 T = -\mathrm{Br}\left[\left(\frac{\partial u}{\partial y}\right)^2 + \left(\frac{\partial u}{\partial z}\right)^2\right], \tag{2}$$

where $u$ and $T$ are the non-dimensional streamwise velocity component and the temperature distribution in the cross-section, respectively. These variables have been non-dimensionalized as $u = u^*/u_w$ and $T = (T^* - T_w)/T_w$, where $u^*$ and $T^*$ are corresponding dimensional quantities. Independent variables are non-dimensionalized using $H$ as a length scale. The dimensionless Laplacian operator $\nabla^2$ has the form $\partial^2/\partial y^2 + \partial^2/\partial z^2$, where $y$ and $z$ represent the directions normal and tangential to the moving surface, respectively. Boundary conditions governing the flow profile are

$$u = 0 \quad \text{at} \quad z = 0, \quad z = \phi, \quad y = 1 \quad \text{and} \quad u = 1 \ \text{at} \ y = 0. \tag{3}$$

Boundary conditions for temperature are

$$T = 0 \quad \text{at} \ z = 0, \quad z = \phi, \quad y = 0, \quad \text{and} \ y = 1, \tag{4}$$

that is, all surfaces of the instrument remain at the reference temperature $T_w$. Equation (4) represents the standard case in which no external heat fluxes are applied [7–10].

The exact solution for Eqs. (1) and (3) can be written for the present coordinate system as [15]

$$u(y,z) = \frac{4}{\pi}\sum_{m=1}^{\infty} \frac{\sin(2m-1)\pi z/\phi \ \sinh(2m-1)\pi(1-y)/\phi}{(2m-1)\sinh(2m-1)\pi/\phi}. \tag{5}$$

Using Eq. (5), $\partial u/\partial y$ and $\partial u/\partial z$ are determined and their squares are used to obtain the viscous dissipation source term in Eq. (2). This procedure yields

$$\nabla^2 T = -\frac{16\ \mathrm{Br}}{\phi^2}\sum_{m=1}^{\infty}\sum_{n=1}^{\infty}\frac{1}{\sinh\ \gamma_m \sinh\ \alpha_n} \times[\sin\ \gamma z_m \sin\ \alpha z_n \cosh\ \gamma_m(1-y)\cosh\ \alpha_n(1-y) + \cos\ \gamma z_m \cos\ \alpha z_n \sinh\ \gamma_m(1-y)\sinh\ \alpha_n(1-y)], \tag{6}$$

where $\gamma_m = (2m-1)\pi/\phi$ and $\alpha_n = (2n-1)\pi/\phi$. Equations (4) and (6) govern the viscous dissipation problem we desire to solve.

## 3 Solution Procedure

Equation (6) is not readily separable. We therefore employ the integral transform [17,18]

$$\overline{T}(y,\beta_j) = \int_0^{\phi} Z(\beta_j, z')T(y,z')dz' \tag{7a}$$

and

$$T(y,z) = \sum_{j=1}^{\infty}\frac{Z(\beta_j,z)\overline{T}(y,\beta_j)}{\int_0^{\phi} Z^2(\beta_j,z')dz'}, \tag{7b}$$

where the overbar notation represents a transform in $z$, eigenvalues are given by $\beta_j$, and $Z(\beta_j, z)$ are corresponding eigenfunctions. As boundary conditions are of the Dirichlet type, eigen-related quantities can be obtained explicitly [19] and are specified by the expressions $\beta_j = j\pi/\phi$ and $Z(\beta_j, z) = \sin\ \beta_j z$.

Equation (6) is transformed using Eq. (7*a*). Regarding the Laplacian operator, $\partial^2 T/\partial y^2$ and $\partial^2 T/\partial z^2$ transform, respectively, as $d^2\overline{T}/dy^2$ and $-\beta_j^2 \overline{T}$. It is necessary to transform the right hand side of the equation on a term-by-term basis. Constants and terms that depend only on $y$ can be moved outside the transformation integral and the equation can be written

$$\frac{d^2\overline{T}}{dy^2} - \beta_j^2\overline{T} = -\frac{16\ \mathrm{Br}}{\phi^2}\sum_{m=1}^{\infty}\sum_{n=1}^{\infty}\frac{1}{\sinh\ \gamma_m \sinh\ \alpha_n} \times\Big[\cosh\ \gamma_m(1-y)\cosh\ \alpha_n(1-y) \times\int_0^{\phi} Z_j' \sin\ \gamma_m z' \sin\ \alpha_n z' dz' + \sinh\ \gamma_m(1-y)\sinh\ \alpha_n(1-y) \times\int_0^{\phi} Z_j' \cos\ \gamma_m z' \cos\ \alpha_n z' dz'\Big], \tag{8}$$

where $Z_j'$ represents a shorthand notation for $Z(\beta_j, z')$. Evaluating the integrals, we find

$$\frac{d^2\overline{T}}{dy^2} - \beta_j^2\overline{T} = -\frac{16\ \mathrm{Br}\ [1-(-1)^j]j}{\phi\pi} \times\sum_{m=1}^{\infty}\sum_{n=1}^{\infty}\frac{1}{\cosh\ b_{mn}\pi/\phi - \cosh\ a_{mn}\pi/\phi} \times\left[\frac{\cosh\ b_{mn}\pi(1-y)/\phi}{j^2 - a_{mn}^2} - \frac{\cosh\ a_{mn}\pi(1-y)/\phi}{j^2 - b_{mn}^2}\right], \tag{9}$$

where $a_{mn} = 2(m-n)$ and $b_{mn} = 2(m+n-1)$. Boundary conditions transform as $\overline{T} = 0$ at $y = 0$ and $y = 1$.

The problem is now posed in terms of non-homogeneous ordinary differential equations for $\overline{T}$. Since coefficients are constant, the method of partial fractions may be used to solve for $\overline{T}$ as the sum of a homogeneous solution $T_H$ and a particular solution $\overline{T_P}$ [20]. The homogeneous component is of the form $T_H = c_1 \cosh\ \beta_j y + c_2 \sinh\ \beta_j y$. If $f(y)$ and $D$ are taken to represent the right hand side of Eq. (9) and $d/dy$, respectively, the equation for the particular solution may be written symbolically as $(D^2 - \beta_j^2)\overline{T_P} = f(y)$. Applying the method of partial fractions results in $T_P = [(D-\beta_j)^{-1} - (D+\beta_j)^{-1}]f(y)/(2\beta_j)$. Integrating this expression and handling evaluation once again on a term-by-term basis for the double series embedded in $f(y)$, we obtain after considerable derivation the particular solution

$$\overline{T}_p = \frac{16\ \mathrm{Br}\,[1-(-1)^j]j\phi}{\pi^3}\sum_{m=1}^{\infty}\sum_{n=1}^{\infty}\frac{\cosh b_{mn}\pi(1-y)/\phi - \cosh a_{mn}\pi(1-y)/\phi}{(\cosh b_{mn}\pi/\phi - \cosh a_{mn}\pi/\phi)(j^2-b_{mn}^2)(j^2-a_{mn}^2)}. \tag{10}$$

Reconstructing the general solution as $\overline{T}=\overline{T}_H+\overline{T}_P$, the integration constants $c_1$ and $c_2$ can be evaluated using the transformed boundary conditions. The result can be written as

$$\overline{T}(y,\beta_j) = \frac{16\ \mathrm{Br}\,[1-(-1)^j]j\phi}{\pi^3}\sum_{m=1}^{\infty}\sum_{n=1}^{\infty}\frac{1}{(j^2-b_{mn}^2)(j^2-a_{mn}^2)} \times\left[\frac{\cosh b_{mn}\pi(1-y)/\phi-\cosh a_{mn}\pi(1-y)/\phi}{\cosh b_{mn}\pi/\phi-\cosh a_{mn}\pi/\phi} - \frac{\sinh j\pi(1-y)/\phi}{\sinh j\pi/\phi}\right]. \tag{11}$$

To obtain the physical solution $T(y,z)$, the inverse transform in Eq. (7*b*) is applied to Eq. (11), yielding

$$T(y,z) = \frac{64\ \mathrm{Br}}{\pi^3}\sum_{j=1,3,5,\ldots}^{\infty} j\ \sin j\pi z/\phi \times\sum_{m=1}^{\infty}\sum_{n=1}^{\infty}\frac{1}{(j^2-b_{mn}^2)(j^2-a_{mn}^2)} \times\left[\frac{\cosh b_{mn}\pi(1-y)/\phi-\cosh a_{mn}\pi(1-y)/\phi}{\cosh b_{mn}\pi/\phi-\cosh a_{mn}\pi/\phi} - \frac{\sinh j\pi(1-y)/\phi}{\sinh j\pi/\phi}\right]. \tag{12}$$

Trivial modes represented by $j=2,4,6,\ldots$, have been removed.

## 4 Results

The Brinkman number appears simply as a scaling factor for the magnitude of $T$ in Eq. (12), while the aspect ratio is embedded within the series. The ratio $T/\mathrm{Br}$ therefore describes the topology of all possible temperature profiles associated with stable flow. Figure 1 shows several examples. Small values of $\phi$ yield asymmetries where maxima are shifted toward the moving surface. This behavior arises in response to the fact that velocity gradients, especially $\partial u/\partial y$, increase near $y=0$ and decrease near $y=1$ as $\phi$ is reduced. These gradient shifts have a commensurate effect upon the dissipation source term in Eq. (6). The degree of asymmetry lessens as the aspect ratio is increased. In the limit $\phi\to\infty$, a parabolic profile is obtained about $y=1/2$ as predicted by standard one-dimensional theory [11].

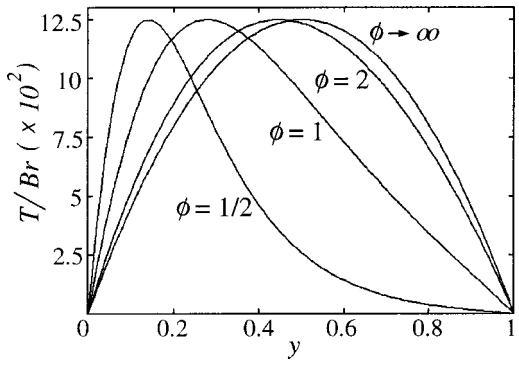


**Fig. 1 Thermal shape profiles ($T/\mathrm{Br}$) at the device centerline ($z=\phi/2$) for aspect ratios 1/2, 1, 2, and ∞**

While Fig. 1 suggests rapid convergence to idealized behavior, it does not quantify error for finite values of $\phi$ when the span is approximated as being infinite. Here, we define an error measure $\varepsilon$ in terms of r.m.s. differences between the idealized profiles [11], $u=1-y$ and $T=\mathrm{Br}\cdot y(1-y)/2$, and their two-dimensional counterparts in Eqs. (5) and (12). Figure 2 shows that both $u$ and $T$ converge logarithmically as functions of $\phi$ to their one-dimensional forms. Notice that contours for $u$ and $T$ coincide at $\mathrm{Br}=5.5$. The hydrodynamic component governs error for $0\leqslant\mathrm{Br}\leqslant 5.5$ because it represents the lower bound for error. Thermal curves for $\mathrm{Br}<5.5$ therefore have no physical significance. Conversely, increased dissipation governs the error for $\mathrm{Br}>5.5$. To a good approximation ($L_\infty\approx 3.5\%$), results in Fig. 2 are described by

$$\varepsilon = 0.16\ \mathrm{Br}\ e^{-1.568\phi}, \tag{13}$$

where $\phi\geqslant 1/2$ and $e$ is the Euler number. That is, Eq. (13) describes the r.m.s. error when using the idealized thermal profile to approximate Eq. (12) and further describes the error when applying the corresponding hydrodynamic idealization to approximate Eq. (5) if Br is set to 5.5.

Because of its logarithmic nature, the actual error will never identically vanish. However, one can choose an appropriate error tolerance below which application of idealized theory is reasonably justified. Strictly speaking, the selected tolerance applies to stable flow only. Any case involving additional higher-order flow modes would likely add a numerical approach and formalized benchmarking would then be required [21]. One can err conservatively by choosing a sufficiently low tolerance, for example, $\varepsilon=10^{-5}$. A neutral curve can then be found which separates the one and two-dimensional models by plotting the locus of points in $(\mathrm{Br},\phi)$ space for this value. This procedure results in the map shown in Fig. 3. The vertical line represents the lower error bound, which is valid for Brinkman numbers up to 5.5. Here, one-dimensional modeling is justified for approximately $\phi\geqslant 7.3$. For $\mathrm{Br}>5.5$, thermal effects govern the problem and the one-dimensional simplification may only be applied at progressively larger aspect ratios. The thermal curve has a steeply increasing slope implying that the required value of $\phi$ is only a weak function of the Brinkman number. This can also be inferred from the close spacing of thermal contours in Fig. 2.

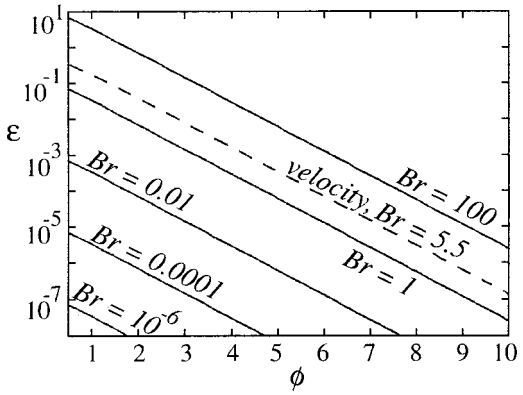


**Fig. 2 Convergence rate of velocity and temperature profiles at the device centerline ($z=\phi/2$) to their one-dimensional forms. Dashed line represents coincident contours for temperature at Br=5.5 and velocity**

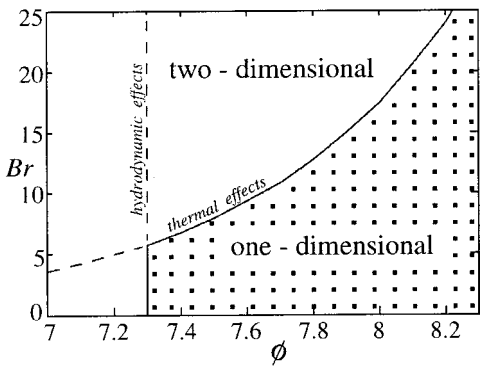


**Fig. 3 Map of parameter space denoting shaded region where idealized theory is permitted within bounds of a $10^{-5}$ r.m.s. error tolerance**

Equations (5) and (12) are predicated upon constant fluid properties. Since the maximum dimensionless temperature rise shown in Fig. 1 is identical for both finite and infinite configurations, the range of applicability of the current model is essentially the same as that for one-dimensional theory [11]. Properly extending the map in Fig. 3 to significantly higher values of Br would require one to consider variable properties, especially viscosity. This would introduce additional material parameters to the problem. Work based upon idealized theory has focused on this issue [7–10], however, we are not aware of any corresponding studies relating to finite devices.

## 5 Conclusion

We have derived the dissipation-dependent temperature distribution for thin-gap Couette flow and used it to analyze finite instruments. This solution can be applied in ways beyond what is discussed here, for example as a numerical test case and/or initial condition for codes designed to simulate heat generating flows.

$\mathrm{Br}$ = Brinkman number $[(\rho \nu u_w^2)/(kT_w)]$
$\mathrm{H}$ = gap size [m]
$\mathrm{L}$ = cylinder span [m]
$\mathrm{T}$ = dimensionless temperature
$T_w$ = reference temperature [K]
$Z$ = eigenfunction
$j,m,n$ = eigenmodes
$k$ = thermal conductivity [W/mK]
$u$ = dimensionless velocity component
$u_w$ = translation speed of rotor surface [m/s]
$y,z$ = dimensionless Cartesian coordinates
$\beta_j$ = eigenvalues
$\varepsilon$ = r.m.s. error
$\phi$ = aspect ratio $[L/H]$
$\nu$ = fluid kinematic viscosity [$\mathrm{m}^2/\mathrm{s}$]
$\rho$ = fluid density [$\mathrm{kg/m}^3$]

## References


[1] Taylor, G. I., 1923, "Stability of a Viscous Liquid Contained Between Two Rotating Cylinders," Philos. Trans. R. Soc. London, Ser. A, **223**, pp. 289–343.
[2] Kobayashi, H., Nashima, T., Okamoto, Y., and Kaminaga, F., 1991, "End Effect in a Coaxial Cylindrical Viscometer," Rev. Sci. Instrum., **62**, pp. 2748–2750.
[3] Ameer, G. A., Barabino, G., Sasisekharan, R., Harmon, W., Cooney, C. L., and Langer, R., 1999, "Ex Vivo Evaluation of a Taylor–Couette Flow, Immobilized Heparinase I Device for Clinical Application," Proc. Natl. Acad. Sci. U.S.A., **96**, pp. 2350–2355.
[4] Criminale, W. O., Jackson, T. L., Lasseigne, D. G., and Joslin, R. D., 1997, "Perturbation Dynamics in Viscous Channel Flows," J. Fluid Mech., **339**, pp. 55–75.
[5] Nagata, M., 1997, "Three-Dimensional Traveling-Wave Solutions in Plane Couette Flow," Phys. Rev. E, **55**, pp. 2023–2025.
[6] Waleffe, F., 1997, "On a Self-Sustaining Process in Shear Flows," Phys. Fluids, **9**, pp. 883–900.
[7] Yueh, C.-S., and Weng, C.-L., 1996, "Linear Stability Analysis of Plane Couette Flow With Viscous Heating," Phys. Fluids, **8**, pp. 1802–1813.
[8] Davis, S. H., Kreigsmann, G. A., Laurence, R. L., and Rosenblat, S., 1983, "Multiple Solutions and Hysteresis in Steady Parallel Viscous Flows," Phys. Fluids, **26**, pp. 1177–1182.
[9] Johns, L. E., and Narayan, R., 1997, "Frictional Heating in Plane Couette Flow," Proc. R. Soc. London, Ser. A, **453**, pp. 1653–1670.
[10] Caridis, K. A., Louwagie, B., and Papathanasiou, T. D., 1997, "Viscous Heating in Planar Couette Flow: Series Solutions for Temperature-Sensitive Fluids," J. Chem. Eng. Jpn., **30**, pp. 123–136.
[11] Bird, R. B., Armstrong, R. C., and Hassager, O., 1977, *Dynamics of Polymeric Liquids*, Wiley, New York.
[12] Benjamin, T. B., 1978, "Bifurcation Phenomena in Steady Flows of a Viscous Fluid II. Experiments," Proc. R. Soc. London, Ser. A, **359**, pp. 27–43.
[13] Benjamin, T. B., and Mullin, T., 1981, "Anomalous Modes in the Taylor Experiment," Proc. R. Soc. London, Ser. A, **377**, pp. 221–249.
[14] Aitta, A., Ahlers, G., and Cannell, D. S., 1985, "Tricritical Phenomena in Rotating Couette-Taylor Flow," Phys. Rev. Lett., **54**, pp. 673–676.
[15] Berker, R., 1963, "Intégration des équations du mouvement d'un fluide visqueux incompressible," in *Handbuch der Physik*, Vol. VIII/2, S. Flügge, ed., Springer-Verlag, Berlin, pp. 1–384.
[16] Schlichting, H., 1979, *Boundary Layer Theory*, McGraw-Hill, New York.
[17] Cotta, R. M., 1993, *Integral Transforms in Computational Heat and Fluid Flow*, CRC Press, Boca Raton.
[18] Wendl, M. C., 1999, "General Solution for the Couette Flow Profile," Phys. Rev. E, **60**, pp. 6192–6194.
[19] Özişik, M. N., 1980, *Heat Conduction*, Wiley, New York.
[20] Sokolnikoff, I. S., and Sokolnikoff, E. S., 1941, *Higher Mathematics for Engineers and Physicists*, McGraw-Hill, New York.
[21] Roache, P. J., 1997, "Quantification of Uncertainty in Computational Fluid Dynamics," Annu. Rev. Fluid Mech., **29**, pp. 123–160.


# Natural Convection in a Cylindrical Enclosure Filled With Heat Generating Anisotropic Porous Medium


**M. R. Dhanasekaran**

**Sarit Kumar Das**

**S. P. Venkateshan**
e-mail: spv35@hotmail.com

Heat Transfer and Thermal Power Laboratory,
Department of Mechanical Engineering,
Indian Institute of Technology Madras,
Chennai-600036, India



*A numerical study has been made to analyze the effects of anisotropic permeability and thermal diffusivity on natural convection in a heat generating porous medium contained in a vertical cylindrical enclosure with isothermal wall and the top and bottom perfectly insulated surfaces. The results show that the anisotropies influence the flow field and heat transfer rate significantly. The non-dimensional maximum cavity temperature increases with increase in permeability ratio. For aspect ratio greater than or equal to two, the nondimensional maximum cavity temperature increases with an increase in the thermal diffusivity ratio. For aspect ratio equal to unity, there exists a critical value of thermal diffusivity ratio at which the maximum cavity temperature is a minimum. This critical value increases with an increase in the value of anisotropic permeability ratio. Based on a parametric study correlations for maximum cavity temperature and average Nusselt number are presented.* [DOI: 10.1115/1.1418700]



Contributed by the Heat Transfer Division for publication in the JOURNAL OF HEAT TRANSFER. Manuscript received by the Heat Transfer Division December 15, 2000; revision received May 30, 2001. Associate Editor: C. Beckerman.

## Introduction

Convective heat transfer in volumetrically heated porous enclosures is of fundamental importance in a number of technological applications such as storage of agricultural products, fermentation process in food industries, packed-bed chemical reactors, nuclear reactor assembly and is also of interest in environmental sciences and geophysics. Much of the work on this topic has been concerned with an isotropic porous medium. Notable among them are the works of Haajizadeh et al. [1] and Prasad [2], on vertical rectangular cavities, Stewart and Dona [3], Prasad and Chui [4] and Rao and Wang [5] on vertical cylinders.

However, in many applications, porous materials are anisotropic, for example, drying of preferentially oriented food grains, columnar dendritic structures formed during solidification of multi-component mixtures, tubular packed bed reactors and rod bundles in a nuclear reactor core. Due to the preferential orientation of the porous matrix in the above applications the permeability and equivalent thermal conductivity of the porous matrix are different in different directions. Only recently, researchers have started investigating natural convection in heat generating anisotropic porous media. Royer and Flores [6] considered natural convection in an anisotropic porous layer inter-bedded horizontally into a homogeneous impermeable medium enclosed in a rectangular enclosure. Parthiban and Patil [7] studied onset of convection in a horizontal layer of heat generating anisotropic porous medium.

The objective of the present work is to study natural convection in a vertical cylindrical enclosure filled with a heat generating porous medium, which is both hydrodynamically and thermally anisotropic. A porous medium is said to be hydro-dynamically anisotropic when it has different permeabilities in different directions whereas it is said to be thermally anisotropic when it has different thermal diffusivities in different directions.

## Mathematical Formulation

The physical system under consideration is a vertical cylinder filled with a porous medium. The wall of the cylinder is considered to be isothermally cooled at $T_c$ while the horizontal surfaces are adiabatic. The porous matrix is both hydrodynamically and thermally anisotropic, and is saturated with an incompressible fluid. The principal directions of the permeabilities ($K$) and effective thermal conductivities ($k$) coincide with the horizontal ($r$) and vertical ($z$) coordinate axes and hence the flow is assumed to be two-dimensional. The thermophysical properties of the fluid and solid matrix are constant except for the fluid density variation in the body force term, i.e., the Boussinesq approximation is employed. The convecting fluid and the porous matrix are in local thermodynamic equilibrium. Darcy's law is assumed to be valid. The heat is generated by a uniformly distributed energy source.

The governing equations for axisymmetric, steady-flow through the porous medium then are

$$\frac{\partial}{\partial r}(ru') + \frac{\partial}{\partial z}(rv') = 0 \tag{1}$$

$$u' = -\frac{K_r}{\mu}\left(\frac{\partial p}{\partial r}\right) \tag{2}$$

$$v' = -\frac{K_z}{\mu}\left[\frac{\partial p}{\partial z} - g\beta(T - T_c)\right] \tag{3}$$

$$u'\frac{\partial T}{\partial r} + v'\frac{\partial T}{\partial z} = \alpha_r\left[\frac{1}{r}\frac{\partial}{\partial r}\left(r\frac{\partial T}{\partial r}\right)\right] + \alpha_z\frac{\partial^2 T}{\partial z^2} + \frac{q'''}{\rho c}, \tag{4}$$

where $K_r$ and $K_z$ are the permeability of the porous medium respectively along the $r$ and $z$ directions; $\alpha_r = k_r/\rho c$ and $\alpha_z = k_z/\rho c$ are the thermal diffusivity of the porous medium respectively along the $r$ and $z$ directions. As $\rho$ and $c$ are assumed to be constant, $\alpha_r$ and $\alpha_z$ are essentially the ratios of thermal conductivities in the $r$ and $z$ directions. In the above $u' = -1/r\partial\psi'/\partial z$ and $v' = 1/r\partial\psi'/\partial r$. By eliminating the pressure term from the momentum equations by cross-differentiation, the governing Eqs. (1)–(4) may be rewritten in the non-dimensional stream-function-temperature form as

$$K^*\frac{\partial}{\partial R}\left[\frac{1}{R}\frac{\partial\psi}{\partial R}\right] + \frac{1}{A^2}\frac{\partial}{\partial Z}\left[\frac{1}{R}\frac{\partial\psi}{\partial Z}\right] = \mathrm{Ra}^*\frac{\partial\theta}{\partial R} \tag{5}$$

$$\frac{\partial\psi}{\partial R}\frac{\partial\theta}{\partial Z} - \frac{\partial\psi}{\partial Z}\frac{\partial\theta}{\partial R} = A\frac{\partial}{\partial R}\left(R\frac{\partial\theta}{\partial R}\right) + \frac{1}{\lambda A}\frac{\partial}{\partial Z}\left(R\frac{\partial\theta}{\partial Z}\right) + 2AR. \tag{6}$$

The dimensionless variables used in writing the above equations are: $R = r/r_0$, $Z = z/H$, $A = H/r_0$ and $\psi = \psi'/\alpha_r r_o$. Since there is no obvious reference temperature difference available, the temperature is non-dimensionalized using the volumetric heat generation rate as $\theta = (T - T_c)/(q''' r_0^2/2k_r)$. As a result of symmetry about the axis of the cylinder, $r = 0$, Eqs. (5) and (6) are solved with the following hydrodynamic and thermal boundary conditions:

$$R = 0,\ \psi = 0,\ \frac{\partial\theta}{\partial R} = 0; \quad R = 1,\ \psi = 0,\ \theta = 0;$$

$$Z = 0,\ \psi = 0,\ \frac{\partial\theta}{\partial Z} = 0; \quad Z = 1,\ \psi = 0,\ \frac{\partial\theta}{\partial Z} = 0.$$

Equations (5) and (6) are solved by the finite volume method as outlined by Gosman et al. [8]. The discretization in this scheme is equivalent to central differences for all terms except the convective term in the energy equation, for which second upwind differencing has been employed. To solve the system of algebraic equations thus obtained, SOR point iterative solver is used that makes use of the new values as soon as they are available. A non-uniform grid field, varying in the form of geometric progression, with very fine grids near the central line and the wall is employed. The adequacy of the grid is verified by comparing the results computed with a $101\times101$ grid with those obtained using a $151\times151$ grid. The difference in maximum non-dimensional temperature and in maximum stream function value for the two grid sizes is within 1 percent. Hence grid size of $101\times101$ has been used for the parametric study. The energy equation is under relaxed at high Rayleigh numbers. A convergence criterion of $10^{-3}$ percent change in both $\psi$ and $\theta$ at all nodes in the domain has been selected to terminate the iterative scheme.

## Results and Discussion

Numerical results for the streamlines, isotherms and Nusselt numbers are obtained for $0.1 \leq K^* \leq 10.0$, $0.1 \leq \lambda \leq 10.0$, $1 \leq A \leq 5$ and $10^2 \leq \mathrm{Ra}^* \leq 10^4$. The range of permeability and thermal diffusivity ratios are chosen based on the work of Neale [9].

**Validation.** The results obtained by the present computational scheme are compared with the results of Rao and Wang [5] and Prasad and Chui [4] in Tables 1 and 2 respectively, which are for an isotropic porous medium. The present results are found to be in good agreement with them.

**Streamlines and Isotherms.** For the case of anisotropic heat generating porous medium representative streamlines and isotherms are shown in Figs. 1 and 2 for $A = 2$ and $\mathrm{Ra}^* = 500$. The flow consists of an asymmetric single cell rotating slowly in the clockwise direction. Figure 1 brings out the effect of permeability ratio on the flow pattern. Figure 1($b$) illustrates the streamlines

**Table 1 Comparison of results with those of Rao and Wang [9]**

| A | $Ra^*$ | $\theta^*_{max}$ | | $\Psi_{min}$ | |
|---|---|---|---|---|---|
| | | Rao and Wang [9] (81 x 81) | Present work (151 x 151) | Rao and Wang [9] (81 x 81) | Present work (151 x 151) |
| 4 | 10 | 0.263 | 0.264 | -0.157 | -0.157 |
| | $1 \times 10^4$ | 0.080 | 0.079 | -25.000 | -24.414 |

Note: $Ra^* = Ra^*/2$, $\theta^*_{max} = \theta_{max}/2$

**Table 2 Comparison of results with those of Prasad and Chui [8]**

| A | $Ra^*$ | $\theta_{max}$ | |
|---|---|---|---|
| | | Present work (151 x 151) | Prasad and Chui [8] (41 x 61) |
| 1 | $1 \times 10^2$ | 0.400 | 0.398 |
| | $1 \times 10^3$ | 0.185 | 0.180 |
| | $1 \times 10^4$ | 0.082 | 0.078 |
| 5 | $1 \times 10^2$ | 0.541 | 0.556 |
| | $1 \times 10^3$ | 0.277 | 0.277 |
| | $1 \times 10^4$ | 0.128 | 0.128 |

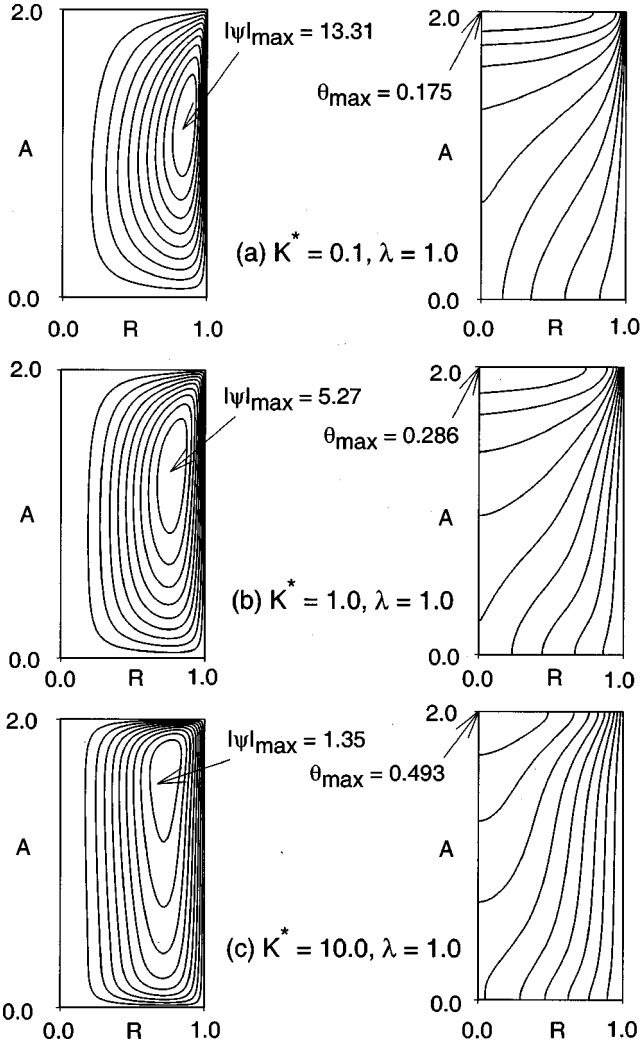


**Fig. 1 Streamline and isotherm plots for different permeability ratios keeping the thermal diffusivity ratio constant at λ=1**

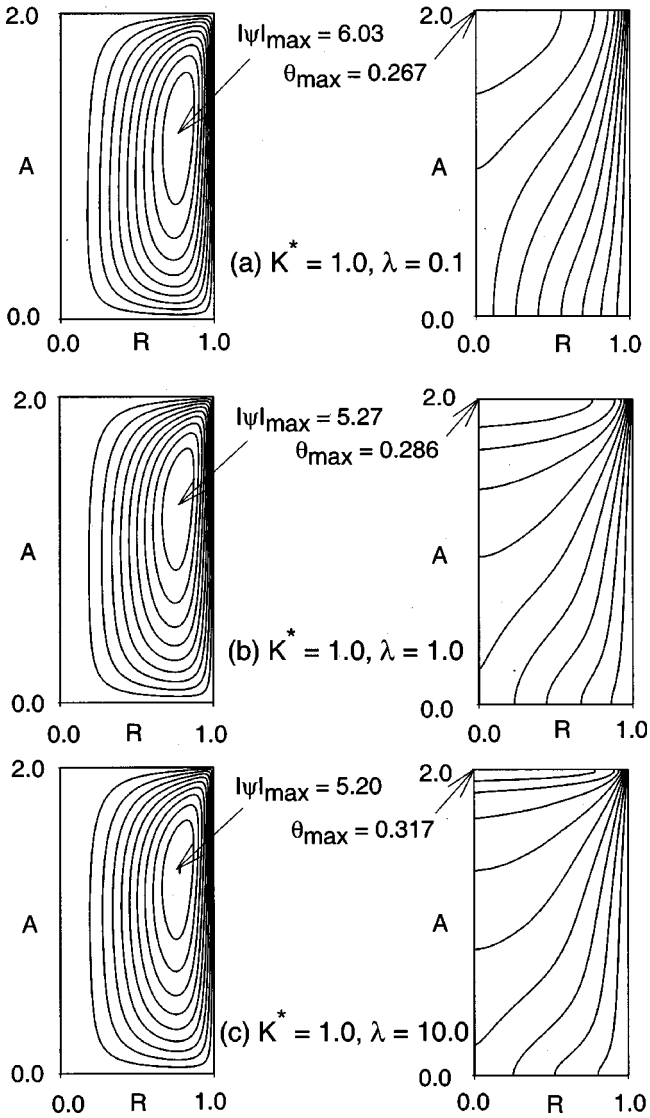


**Fig. 2 Streamlines and isotherms for different thermal diffusivity ratios keeping the permeability ratio constant at $K^*=1$**

and isotherms for the isotropic case (i.e., $K^*=\lambda=1.0$). Sharp gradients in velocity and temperature are observed near the isothermally cooled side wall. Temperature stratification is observed in the upper portion of the cylinder. Figure 1(*a*) shows the streamlines and isotherms for $K^*=0.1$ and $\lambda=1.0$ (i.e., the permeability in the vertical direction is greater than that in the horizontal direction). The buoyancy induced flow along the isothermal cold wall is much stronger for this case than for $K^*=1.0$. The flow channels along the side wall. When compared to isotropic case the extent of thermally stratified zone increases.

The opposite extreme is shown in Figure 1(*c*). For $K^*=10.0$ and $\lambda=1.0$, no sharp gradients in velocity and temperature are observed near the side wall, while the horizontally flowing fluid channels along the top and bottom adiabatic walls. This practically induces the so called ''plug flow'' in the fluid. Due to the relatively low permeability in the vertical direction, the intensity of natural convection flow is very weak as compared to isotropic permeability case. Also the flow outside the ''horizontal channels'' is very nearly parallel to the vertical wall. Once the fluid reaches the top or bottom adiabatic wall, it bends sharply and merges into

the fast flowing fluid in the horizontal channels. Consequently, the isotherms are almost vertical, indicating that heat transfer across the enclosure is mostly by conduction.

Figure 2 shows the effect of thermal diffusivity ratio via streamline and isotherm plots for $K^*=1.0$. For $\lambda=0.1$ (Fig. 2(*a*)), the thermal diffusivity is much higher in the vertical direction than in the horizontal direction. Hence the temperature gradient in the vertical direction is observed to be smaller than that for $\lambda=1.0$ case. However, the flow intensity is slightly higher than that for $\lambda=1.0$. As shown in Fig. 2(*b*) and 2(*c*), increase in thermal diffusivity ratio has virtually no effect on the flow pattern. Due to the relatively low thermal diffusivity in the vertical direction, the temperature stratification in the vertical direction is stronger for $\lambda=10.0$ than that for $\lambda=1.0$.

**Centerline Temperature Distribution.** Figure 3 presents the temperature distribution on the centerline of the cylinder for three different permeability ratios while keeping the diffusivity ratio constant at $\lambda=1$ and also for three different thermal diffusivity ratios while keeping the permeability ratio constant at $K^*=1.0$. As the permeability ratio decreases (i.e., the permeability in the vertical direction is larger than that in the horizontal direction), the dimensionless temperature $\theta_o$ is observed to be less than that in the isotropic case due to stronger buoyancy. As the permeability ratio increases (i.e., the permeability in the horizontal direction is larger than that in the vertical direction), the dimensionless temperature $\theta_o$ is found to be higher than the isotropic case. Also, the larger the permeability ratio, the larger is the temperature gradient $\partial\theta_o/\partial Z$ at any height $Z$.

When the thermal diffusivity ratio is above unity, the dimensionless temperature $\theta_o$ is observed to be less than the isotropic case everywhere except in a small region near the top adiabatic wall. Due to the relatively smaller thermal diffusivity in the vertical direction, there exists a very large temperature gradient, which results in the temperature exceeding that of the isotropic case, near the top adiabatic wall. As the thermal diffusivity ratio is reduced below unity, the centerline temperature is observed to be higher than the isotropic case everywhere except in a small region close to the top adiabatic wall. Due to the relatively larger thermal diffusivity in the vertical direction, a smaller temperature gradient exists in the vertical direction such that the temperature falls below the isotropic value near the top adiabatic wall.

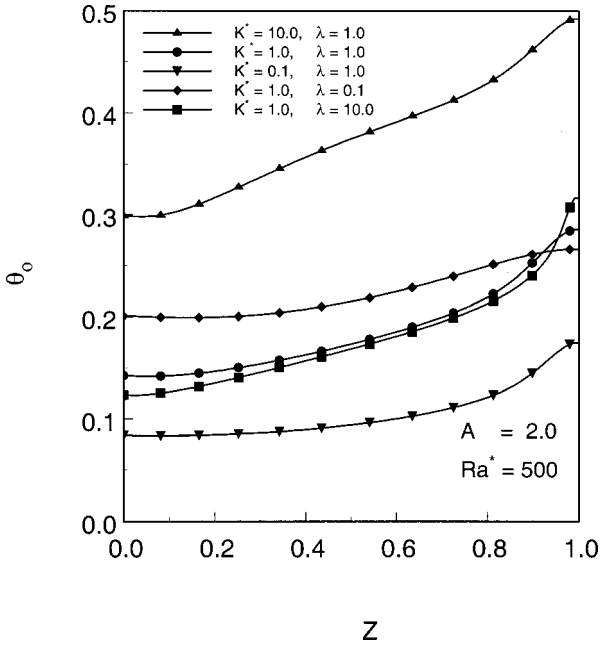


**Fig. 3 Effect of permeability ratio and thermal diffusivity ratio on centerline temperature distribution**

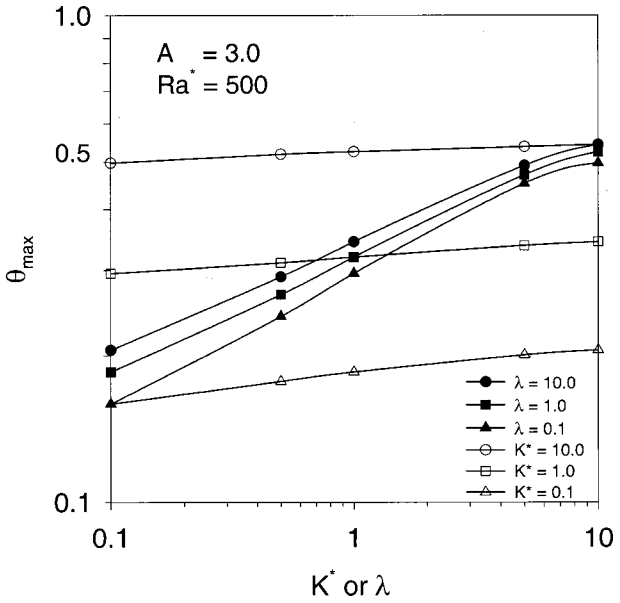


**Fig. 4 Effect of permeability ratio and thermal diffusivity ratio on the maximum temperature for $A\geqslant 2$**

**Maximum Temperature.** Figure 4 shows the effect of permeability ratio and thermal diffusivity ratio on non-dimensional maximum temperature $\theta_{\max}$. For the entire range of aspect ratios, $\theta_{\max}$ increases with an increase in permeability ratio because of fluid flow channeling along the horizontal walls and also because of reduced flow velocity everywhere in the cavity. (Refer to Fig. 1 also). $\theta_{\max}$ varies linearly with the permeability ratio for the range of permeability ratio considered in the present work. When $K^*\rightarrow 10$, $\theta_{\max}$ is observed to approach the pure conduction value. For $A\geqslant 2$, $\theta_{\max}$ is observed to increase linearly with thermal diffusivity ratio. However, it is evident that the effect of thermal diffusivity ratio on $\theta_{\max}$ is not as severe as that of permeability ratio. Effect of permeability ratio and thermal diffusivity ratio on $\theta_{\max}$ presented in Fig. 5 for $A=1$ shows an interesting feature. Though $\theta_{\max}$ increases with an increase in permeability ratio, the variation is non-linear. However, the variation is linear for higher aspect ratios ($A\geqslant 2$) as shown in Fig. 4. For a given permeability ratio, there exists a critical value of $\lambda$ at which $\theta_{\max}$ becomes a minimum. However the difference between the maximum and minimum is within $\pm 10.0$ percent of the mean value for the range of $\lambda$ considered in the present study. This critical value of $\lambda$ increases with an increase in $K^*$. Existence of a critical value of $\lambda$ with respect to the variation of Nusselt number has been reported earlier by Chang and Lin [10] for anisotropic porous medium without heat generation.

The maximum temperature can be correlated in terms of aspect ratio, Rayleigh number and for the first time, permeability ratio and thermal diffusivity ratio as

$$\theta_{\max}=1.778\mathrm{Ra}^{*-0.325}A^{0.259}K^{*0.271}\lambda^{0.028} \tag{7}$$

for the range $1\times 10^3\leqslant \mathrm{Ra}^*\leqslant 1\times 10^4$, $2\leqslant A\leqslant 5$, $0.1\leqslant K^*\leqslant 10.0$, and $0.1\leqslant\lambda\leqslant 10.0$. The correlation coefficient and the average error for the correlation are 0.998 and $\pm 3.23$ percent respectively, which show the goodness of the fit.

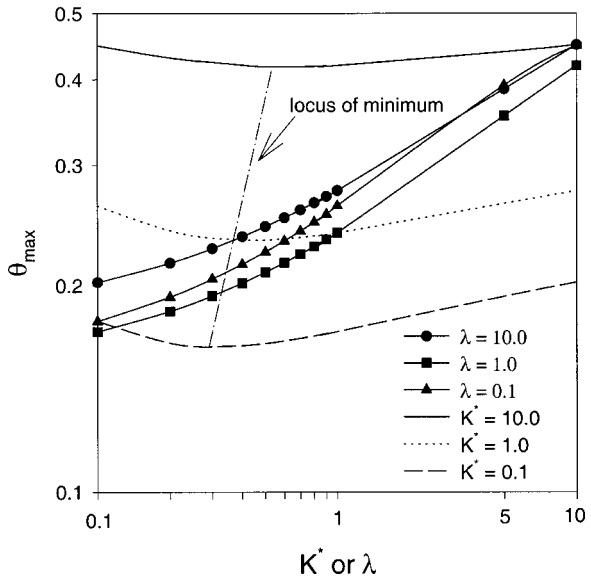


**Fig. 5 Effect of permeability ratio and thermal diffusivity ratio on the maximum temperature for $A=1.0$**

**Overall Heat Transfer.** For the problem considered here, there is no well-defined characteristic temperature difference to express the heat transfer coefficient. However, one can define an overall Nusselt number based on the mean temperature on the centerline. When the heat transfer coefficient is defined in terms of $(T_m-T_c)$, the overall Nusselt number is obtained as $\mathrm{Nu}_{av}=h_{av}r_o/k_r=1/\theta_m$. The overall Nusselt number can thus be correlated as

$$\mathrm{Nu}_{av}=0.556\mathrm{Ra}^{*0.396}A^{-0.233}K^{*-0.338}\lambda^{0.032}, \qquad (8)$$

for the range $1\times10^3\leq\mathrm{Ra}^*\leq1\times10^4$, $2\leq A\leq5$, $0.1\leq K^*\leq10.0$, and $0.1\leq\lambda\leq10.0$. The correlation coefficient and the average error for the correlation are 0.998 and $\pm3.34$ percent respectively, which show the goodness of the fit.

## Conclusions

A numerical study has been performed of natural convection in a cylindrical cavity filled with a heat generating anisotropic porous medium. A low permeability ratio ($K^*<1$) causes channeling of the flow along the isothermal vertical wall and a higher flow intensity in the enclosure. A large permeability ratio ($K^*>1$) causes channeling of the flow along the horizontal adiabatic walls and a lower flow intensity in the enclosure. A low thermal diffusivity ratio ($\lambda<1$) causes a slightly higher flow intensity in the enclosure. A large thermal diffusivity ratio ($\lambda>1$) has little effect on the flow pattern or flow intensity in the enclosure. As permeability ratio increases maximum cavity temperature increases, for the entire range of aspect ratio studied. For $A\geq2$, larger the thermal diffusivity ratio, larger is the maximum cavity temperature. For $A=1$, there exists a critical value of thermal diffusivity ratio at which the maximum cavity temperature is minimum. This critical value increases with an increase in permeability ratio. General correlations for maximum cavity temperature and average Nusselt number are presented in terms of Rayleigh number, aspect ratio, permeability ratio and thermal diffusivity ratio.

## Nomenclature

$A$ = aspect ratio, $H/r_o$
$g$ = acceleration due to gravity, m/s$^2$
$H$ = cylinder height, m
$h$ = heat transfer coefficient, W/m$^2$K
$K$ = porous medium permeability, m$^2$
$K^*$ = anisotropic permeability ratio, $K_r/K_z$
$k$ = porous medium effective thermal conductivity, W/mK
Nu = Nusselt number based on cylinder radius, $hr_o/k_r$
$p$ = pressure, Pa
$q'''$ = volumetric heat generation rate, W/m$^3$
$r$ = radial co-ordinate, m
$R$ = dimensionless distance in radial direction, $r/r_o$
$r_o$ = cylinder radius, m
Ra* = Darcy modified Rayleigh number, $g\beta K_r r_o(q'''r_0^2/2k_r)/\nu\alpha_r$
$T$ = temperature, K
$u'$, $v'$ = fluid velocity in the $r$ and $z$ directions, m/s
$z$ = axial co-ordinate, m
$Z$ = dimensionless distance in the axial direction, $z/H$

### Greek Symbols

$\alpha$ = thermal diffusivity, m$^2$/s
$\beta$ = isobaric coefficient of volumetric thermal expansion, 1/K
$\lambda$ = anisotropic thermal diffusivity ratio, $\alpha_r/\alpha_z$
$\theta$ = dimensionless temperature, $(T-T_c)/(q'''r_o^2/2k_r)$
$\mu$ = dynamic viscosity, Ns/m$^2$
$\nu$ = kinematic viscosity, m$^2$/s
$\rho$ = fluid density, kg/m$^3$
$\psi'$ = stream function, m$^3$/s
$\psi$ = dimensionless stream function, $\psi'/\alpha_r r_o$

### Subscripts

$av$ = average
$c$ = cold vertical wall
$m$ = averaged along the line of symmetry
max = maximum
$o$ = line of symmetry ($r=0$)
$r$, $z$ = radial and axial directions
$z$ = axial direction

## References

[1] Haajizadeh, M., Ozgue, A. F., and Tien, C. L., 1984, "Natural Convection in a Vertical Porous Enclosure With Internal Heat Generation," Int. J. Heat Mass Transf., **27**, pp. 1893–1902.
[2] Prasad, V., 1987, "Thermal Convection in a Rectangular Cavity Filled With a Heat Generating, Darcy Porous Medium," ASME J. Heat Transfer, **109**, pp. 697–703.
[3] Stewart, W. E., Jr., and Dona, C. L. G., 1988, "Free Convection in a Heat Generating Porous Medium in a Finite Vertical Cylinder," ASME J. Heat Transfer, **110**, pp. 517–520.
[4] Prasad, V., and Chui, A., 1989, "Natural Convection in a Cylindrical Porous Enclosure With Internal Heat Generation," ASME J. Heat Transfer, **111**, pp. 916–925.
[5] Rao, Y. F., and Wang, B. X., 1991, "Natural Convection in Vertical Porous Enclosures With Internal Heat Generation," Int. J. Heat Mass Transf., **34**, pp. 247–252.
[6] Royer, J. J., and Flores, L., 1994, "Two-Dimensional Natural Convection in an Anisotropic and Heterogeneous Porous Medium With Internal Heat Generation," Int. J. Heat Mass Transf., **37**, pp. 1387–1399.
[7] Parthiban, C., and Patil, P. R., 1997, "Thermal Instability in an Anisotropic Porous Medium With Internal Heat Source and Inclined Temperature Gradient," Int. Commun. Heat Mass Transfer, **24**, pp. 1049–1058.
[8] Gosman, A. D., Pun, W. M., Runchal, A. K., Spalding, D. B., and Wolfshtein, M., 1969, *Heat and Mass Transfer in Recirculating Flows*, Academic Press, London.
[9] Neale, G., 1977, "Degrees of Anisotropy for Fluid Flow and Diffusion Through Anisotropic Porous Media," AIChE J., **23**, pp. 56–62.
[10] Chang, W. J., and Lin, H. C., 1994, "Natural Convection in a Finite Wall Rectangular Cavity Filled With an Anisotropic Porous Medium," Int. J. Heat Mass Transf., **37**, pp. 303–312.

# Application of Differential Transform Method to Heat Conduction in Tapered Fins

**Charles W. Bert**
School of Aerospace and Mechanical Engineering, The University of Oklahoma, Norman, OK 73019-1052
e-mail: cbert@ou.edu

*This paper analyzes steady-state heat conduction in a triangular-profile fin using a relatively new, exact series method of solution known as the differential transform method. This method converges with only six terms or less for the cases considered. Its advantage is that, unlike many popular methods, it is an exact method and yet it does not require the use of Bessel or other special functions.* [DOI: 10.1115/1.1423316]

*Keywords: Computational, Finned Surfaces Heat Transfer, Temperature, Heat Conduction*

## Introduction

Zhou [1] introduced a method, based on Taylor series expansion, for solving initial-value problems of electrical circuits. He named the method *differential transformation*. Later, Chen and Ho [2] applied the differential transformation (DT) method to solution of second-order eigenvalue problems. Recently Malik and Dang [3] first applied the DT method to vibration analysis, specifically the fourth-order system for vibration of prismatic beams.

After completing the present work, the author learned, from one of the reviewers, of previous work by Yu and Chen [4]. They dealt with determination of the optimal length for circular fins of rectangular profile. They considered thermal conductivity varying with temperature, heat transfer coefficient varying with radial position and nonlinear conducting-convecting-radiating heat transfer. Solution was by a domain version of the differential transformation method, although few details were given regarding accuracy.

The present paper considers steady-state heat transfer in a triangular-profile fin with constant properties and gives details of application of the method as well as a convergence study.

## The Boundary-Value Problem

Let $x$ be the position coordinate along the axis of the fin (normalized by the length $L$) and $\theta$ dimensionless temperature above ambient. The cross-sectional area of the fin varies linearly with $x$, measured from the apex. Then the governing differential equation is the following second-order equation with varying coefficients (Arpaci, [5])

$$x\frac{d^2\theta}{dx^2}+\frac{d\theta}{dx}-m^2\theta=0, \tag{1}$$

where $\theta$ is the temperature measured above ambient and normalized by the base temperature, and $m^2$ is a fin parameter given by

$$m^2=(h_1+h_2)AR/k.$$

Here $AR$ is the plate aspect ratio (length /depth), $h_1$ and $h_2$ are the convective heat transfer coefficients of the top and bottom surfaces, and $k$ is the thermal conductivity.

The boundary conditions are no heat flux at the tip

$$\lim_{x\to 0}\left(x\frac{d\theta}{dx}\right)=0, \tag{2}$$

and a dimensionless temperature of unity at the base ($x=1$), i.e.,

$$\theta(1)=1. \tag{3}$$

## Differential Transformation Method

An arbitrary function $f(x)$ can be expanded in a Taylor series about a point $x=0$ as

$$f(x)=\sum_{k=0}^{\infty}\frac{x^k}{k!}\left[\frac{d^ku}{dx^k}\right]_{x=0}. \tag{4}$$

The differential transformation of $f(x)$ is defined as

$$F(k)=\frac{1}{k!}\left[\frac{d^ku}{dx^k}\right]_{x=0}. \tag{5}$$

Then the inverse differential transformation is

$$f(x)=\sum_{k=0}^{\infty}x^kF(k). \tag{6}$$

Before taking the differential transformation of each term in Eq. (1), we note that

$$x\to\delta(k-1)=\{1\ \text{ if }\ k=1\ \text{ otherwise }\ 0$$

$$\frac{d^n\theta}{dx^n}\to\frac{(n+k)!}{k!}T(n+k),$$

where $T(k)$ is the differential transform ($DT$) of $\theta(x)$.

$$f(x)\theta(x)\to\sum_{l=0}^{k}F(l)T(k-l),$$

where $F(k)$ is the $DT$ of $f(x)$.
For the first term in Eq. (1), $f(x)$ is simply $x$ and $n=2$. Thus,

$$x\frac{d^2\theta}{dx^2}\to\sum_{l=0}^{k}\delta(l-1)(k-l+1)(k-l+2)T(k-l+2).$$

For the second term in Eq. (1),

$$\frac{d\theta}{dx}\to(k+1)T(k+1),$$

and for the third term,

$$-m^2\theta(x)\to-m^2T(k).$$

Thus, the transformed version of Eq. (1) is

$$\sum_{l=0}^{k}\delta(l-1)(k-l+1)(k-l+2)T(k-l+2)$$
$$+(k+1)T(k+1)-m^2T(k)=0. \tag{7}$$

The transformed boundary conditions are

$$\sum_{l=0}^{k}\delta(l-1)(k+1)T(k+1)=0 \tag{8}$$

$$\sum_{l=0}^{k}T(k)=1. \tag{9}$$

Expanding the boundary condition Eq. (8) for various $k$ values, one can obtain all the $T(k)$ values as zero which is a trivial solution. However, the solution as given by $DT$ method Eq. (6) automatically satisfies this boundary condition as $x\to 0$. In other words, the physical significance is that as $x\to 0$, all the coefficients of $d\theta/dx$ should be finite. As there are no negative powers

Contributed by the Heat Transfer Division for publication in the JOURNAL OF HEAT TRANSFER. Manuscript received by the Heat Transfer Division January 12, 2001; revision received August 15, 2001. Associate Editor: G. S. Dulikravich.

  

of $x$ in Eq. (6) the coefficients $T(k)$ are indeed finite and the boundary condition is automatically satisfied. For the case of tapered fins having both ends of finite thickness, this boundary condition is necessary to solve the problem completely.

Successive applications of Eq. (7) yield

$$k=0: \quad T(1)-m^2T(0)=0 \quad \text{or} \quad T(1)=m^2T(0)$$

$$k=1: \quad 2T(2)+2T(2)=m^2T(1).$$

Thus,

$$T(2)=(m^2/4)T(1)=(m^4/4)T(0)$$

$$k=2: \quad 6T(3)+3T(3)=m^2T(2).$$

Thus,

$$T(3)=(1/9)m^2T(2)=(m^6/36)T(0).$$

Inserting the above expressions for $T(0)$ through $T(3)$ into Eq. (9) and solving for $T(0)$ yields

$$T(0)=\frac{1}{1+m^2+(m^4/4)+(m^6/36)}. \tag{10}$$

## Numerical Results

For $m^2=1$, Eq. (10) yields $T(0)=0.439024$, which is only 0.079 percent higher than 0.4386734, the exact Bessel function solution.

Once the various values of $T(k)$ are known, the dimensionless temperature distribution is given by Eq. (6) converted to the notation of the present problem:

$$\theta(x)=\sum_{k=0}^{\infty} x^kT(k). \tag{11}$$

For the present case, up to third order,

$$\theta(x)=T(0)+xT(1)+x^2T(2)+x^3T(3).$$

For the case of $m^2=1$, the dimensionless temperature at the mid-point ($x=1/2$) is 0.6874993, which is 0.0717 percent higher than the exact solution. Fin efficiency $\eta$ is defined as the ratio of the actual heat transfer rate through the base of a fin to that of an ideal fin having a uniform temperature equal to the base temperature of the actual fin. Fin efficiency is probably a better measure of the accuracy of the method than the temperature values mentioned above. For $m^2=1$, the *DT* method gives $\eta=69.5$ percent or 0.372 percent lower than the exact value.

**Table 1 Root and mid-point temperatures and fin efficiency as a function of parameter *m* using only three terms (% error in parentheses)**

| m | 0.25 | 0.5 | 0.75 | 1.0 | 1.5 | 2.0 |
|---|---|---|---|---|---|---|
| T(0) | 0.9403 (0.0) | 0.7898 (0.0) | 0.6073 (0.016) | 0.439 (0.079) | 0.2069 (1.025) | 0.09278 (4.95) |
| T(1/2) | 0.9699 (0.0) | 0.8916 (0.0) | 0.7904 (0.0) | 0.6874 (0.0717) | 0.5133 (0.864) | 0.3917 (4.12) |
| Fin Efficiency, % | 96.99 (-0.01) | 89.26 (-0.022) | 79.41 (-0.088) | 69.51 (-0.372) | 52.7 (-2.389) | 40.2 (-6.892) |

**Table 2 Exact values and the number of terms required to obtain them, as a function of parameter *m***

| m | 0.25 | 0.5 | 0.75 | 1.0 | 1.5 | 2.0 |
|---|---|---|---|---|---|---|
| T(0) | 0.9403 | 0.7898 | 0.6072 | 0.4386 | 0.2048 | 0.0884 |
| T(1/2) | 0.9699 | 0.8916 | 0.7904 | 0.6868 | 0.5089 | 0.3765 |
| Fin Efficiency % | 96.99 | 89.26 | 79.48 | 69.74 | 53.98 | 43.13 |
| Number of Terms | 3 | 3 | 4 | 4 | 5 | 6 |

Table 1 summarizes the end and mid point temperatures along with fin efficiency for various values of $m$ with three terms and Table 2 gives the number of terms required to converge to an exact solution up to five significant digit accuracy.

## Conclusion

The advantage of the *DT* method over other methods, such as the ordinary and variational heat balance integral method, the ordinary and improved Rayleigh method, and the mean-square error method [6], is that the *DT* method is exact. Nevertheless it is rather straight forward to apply.


## Acknowledgment

The author acknowledges the computations performed by Krishna K. Devarakonda.


## References


[1] Zhou, J. K., 1986, *Differential Transformation and its Application for Electrical Circuits* (in Chinese), Huazhong University Press, Wuhan, P. R. China.

[2] Chen, C. K., and Ho, S. H., 1996, "Application of Differential Transformation to Eigenvalue Problems," Appl. Math. Comput., **79**, pp. 173–188.

[3] Malik, M., and Dang, H. H., 1998, "Vibration of Continuous Systems by Differential Transformation," Appl. Math. Comput., **96**, pp. 17–26.

[4] Yu, L. T., and Chen, C. K., 1999, "Optimization of Circular Fins with Variable Thermal Parameters," J. Franklin Inst., **336B**, pp. 77–95.

[5] Arpaci, V. S., 1966, *Conduction Heat Transfer*, Addison-Wesley, Reading, MA, p. 150.

[6] Bert, C. W., 1986, "Improved Approximate Methods for Analyzing Steady Heat Conduction," Commun. Appl. Numer. Methods, **2**, pp. 587–592.


# Laminar Mixed Convection Adjacent to Three-Dimensional Backward-Facing Step


**A. Li and B. F. Armaly**

Department of Mechanical and Aerospace Engineering and Engineering Mechanics, University of Missouri-Rolla, Rolla, MO 65409



*Simulations of three-dimensional laminar buoyancy-assisting mixed convection adjacent to a backward-facing step in a vertical rectangular duct are presented to demonstrate the influence of Grashof number on the distributions of the Nusselt number, and the reverse flow regions that develop adjacent to the duct's walls. The Reynolds number, and duct's geometry are kept constant: heat flux at the wall downstream from the step is kept uniform but its magnitude varied to cover a Grashof number range of 0–4000; all the other walls in the duct are kept at adiabatic condition; and the flow, upstream of the step, is treated as fully developed and isothermal. Increasing the Grashof number results in increasing the Nusselt number; the size of the secondary recirculation flow region adjacent to the stepped wall; the size of the reverse flow region adjacent to the sidewall and the flat wall; and the spanwise flow from the sidewall toward the center of the duct. On the other hand, the size of the primary recirculation flow region adjacent to the stepped wall decreases and detaches partially from the heated stepped wall as the Grashof number increases. Details are presented and discussed.* [DOI: 10.1115/1.1423909



*Keywords: Convection, Finite Volume, Mixed Convection, Separated, Three-Dimensional*

Contributed by the Heat Transfer Division for publication in the JOURNAL OF HEAT TRANSFER. Manuscript received by the Heat Transfer Division March 27, 2001; revision received October 5, 2001. Associate Editor: M. Faghri.

## Introduction

Separated and reattached flow occurs in many heat-exchanging devices, such as electronic and power generating equipment and dump combustors. A great deal of mixing of high and low energy fluid occurs in the separated and reattached flow regions, thus impacting significantly the heat transfer performance of these devices. Studies have been conducted extensively during the past decade, and the backward facing step geometry received most of the attention [1–3]. The majority of published work dealt with the two-dimensional isothermal flow behavior, and comparatively little is published about the three-dimensional non-isothermal case. Forced convection results have been reported for a duct with an aspect ratio of 16 by Iwai et al. [4], with an aspect ratio of 12 by Pepper and Carrington [5], and with an aspect ratio of 8 by Armaly et al. [6]. The numerical study of Iwai et al. [7] established that an aspect ratio greater than 16 is needed to maintain a small two-dimensional region near the centerline of the duct with expansion ratio of 2 at Reynolds number of 250, and for higher Reynolds number the flow becomes three-dimensional throughout the duct. To the authors' knowledge the work of Iwai et al. [8] on the effects of inclination angle on the heat transfer for a duct with aspect ratio of 16, and the work of Li and Armaly [9] on mixed convection in a duct with aspect ratio of 8 are the only published three-dimensional results that incorporate the buoyancy force in the analysis.

## Model Description and Simulation

Three-dimensional laminar buoyancy-assisting convection flow in a heated duct with a backward-facing step is numerically simulated and the computation domain is shown in Fig. 1. The upstream height of the duct ($h$) is 0.01 m, its downstream height ($H$) is 0.02 m, and its width is ($W$) is 0.08 m. This geometry provides a backward facing step height of $S=0.01$ m, an expansion ratio of $ER=H/(H-S)=2$, and an aspect ratio of $AR=W/S=8$. By exploiting the symmetry of the flow field in the spanwise direction, the width of the computation domain was reduced to half of the actual width of the duct ($L=0.04$ m). The length of the computation domain is 0.02 m and 0.5 m upstream and downstream of the step respectively, i.e., $-2\leqslant x/S\leqslant 50$. The origin of the coordinate system is located at the bottom corner of the step as shown in Fig. 1. The governing equations for laminar buoyancy assisting mixed convection flow (with gravity, $g$, in the streamwise direction) with constant properties under steady conditions are formulated for continuity, momentum and energy conservation. Thermal buoyancy effects are modeled using the Boussinesq approximation. The full elliptic three-dimensional coupled governing equations are solved using finite volume method to simulate the thermal and the flow field (where $T$ is temperature and $u$, $v$, $w$ are velocity components in coordinate direction $x$, $y$, and $z$ as shown in Fig. 1) in this geometry. Details of the formulation are given by Li and Armaly [9]. The physical properties are treated as constants in the simulations and evaluated for air at the inlet temperature of $T_0=20$°C (i.e., density ($\rho$) equals to 1.205 kg/m$^3$, dynamic viscosity ($\mu$) is $1.81\times10^{-5}$ kg/m·s, thermal conductivity ($k$) is 0.0259 W/m·°C, specific heat ($C_p$) is 1005 J/kg°C, and volumetric coefficient of thermal expansion ($\beta$) is 0.00341 1/K). The boundary conditions are treated as no slip conditions at the solid walls, and adiabatic at all the walls with the exception of the downstream stepped wall ($y/S=0.0$ m, for $0.0\leqslant x/S\leqslant 50$, and all $z$) that was treated as having a uniform heat flux ($q_w=-k\partial T/\partial y|_{y=0}$). The uniform heat flux at the downstream stepped wall is varied while keeping the flow rate constant (Reynolds number, $\mathrm{Re}=2\rho u_0 h/\mu=200$, where $u_0$ is the average inlet velocity in the upstream section of the duct) in order to investigate the effects of the buoyancy force (the Grashof number, $\mathrm{Gr}=\rho^2 g\beta q_w S^4/\mu^2 k$, and $0.0\leqslant \mathrm{Gr/Re}^2\leqslant 0.1$) on the flow and heat transfer behavior. Symmetry conditions were imposed at the center width of the duct ($z/L=1$, for all $x$ and $y$), and fully developed conditions were imposed at the outlet ($x/S=50$, for all $y$ and $z$) and inlet planes ($x/S=-2$, $1\leqslant y/S\leqslant 2$, for all $z$) of the computation domain.

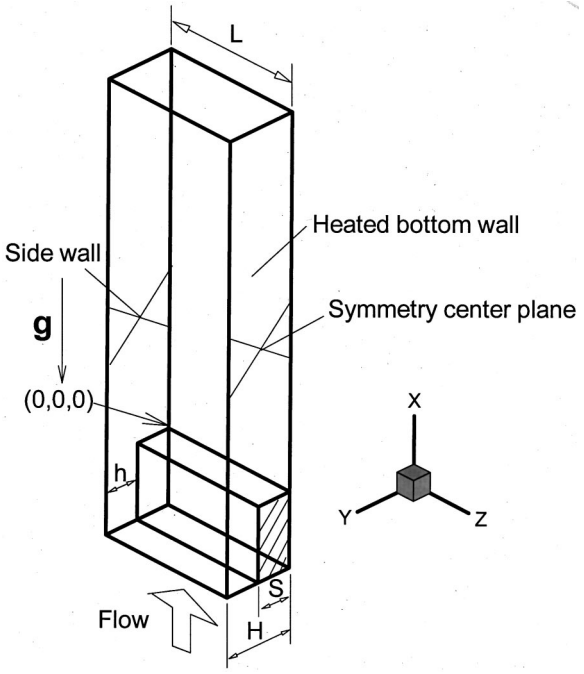


**Fig. 1 Schematic of the computation domain**

Hexahedron volume elements are used in the simulations. The convergence criterion required that the scaled residuals be smaller than $10^{-4}$ for the continuity and the momentum equations and smaller than $10^{-6}$ for the energy equation. All of the calculations were performed on HP Visualine C200 workstations, and the CPU time for converged solution is approximately five hours. Detailed descriptions of the CFD code and the solution procedure can be found in the FLUENT manual. The grid was generated to insure high density close to the walls and the step, where high gradients are expected, in order to insure the accuracy of the simulation. Grid independence tests were performed for the case with Reynolds number of Re=400, and wall heat flux of $q_w=21.19$ W/m$^2$. Comparisons of the results for the minimum and maximum temperature on the downstream stepped wall, reattachment length at the center of the duct and the minimum reattachment length are conducted for different grid densities downstream of the step, $100(x)\times20(y)\times20(z)$, $125\times25\times25$, $150\times30\times30$, and $180\times35\times35$, respectively. The results show that for the larger grid ($180\times35\times35$), the differences are less than 1 percent for the temperature and reattachment length. A grid of $150\times30\times30$ downstream of the step and a grid of $20\times15\times30$ upstream of the step are selected for this simulation.

## Results and Discussion

The present study is an extension to the one reported by Armaly et al. [6], dealing with the forced convection in the same duct geometry. The "jet like" flow that develops near the sidewall within the separating shear layer, and the reverse flow that develops adjacent to the sidewall are the major three-dimensional flow features in this geometry. These features also dominate the flow and heat transfer behavior in mixed convection. The focus of this study is on examining and quantifying the effects of the buoyancy force (Gr) on the flow and heat transfer characteristics.

Impingement of the "jet like" flow on the stepped wall is responsible for creating a minimum in the spanwise distribution of the reattachment line, along with a maximum in the Nusselt num-

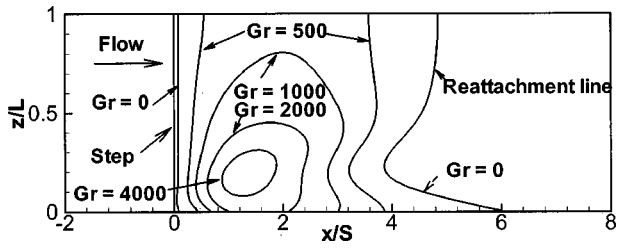


**Fig. 2 Effects of Grashof number on the distribution of the reattachment line**

ber distribution near the sidewall. Spanwise distributions of reattachment line (as defined by the locations where $\partial u/\partial y|_{y=0}$) for the primary and secondary recirculation flow regions are presented in Fig. 2 for different Grashof numbers. The minimum that occurs in that distribution near the sidewall can be seen clearly for Gr=0 and 500. The maximum length of the primary recirculation flow region occurs at the sidewall and not, as expected, at the center of the duct. As the Grashof number increases, i.e., Gr=500, the primary reattachment line moves closer to the step, and the secondary reattachment line moves away from the step. This means that the size of the secondary and the primary recirculation flow regions increase and decrease, respectively, as the Grashof number increases. The figure shows that the primary recirculation flow region is partially lifted away from the heated stepped wall and the secondary recirculation flow region is vented to the main flow at the center of the duct for Gr=1000. The size of that lifted region increases with increasing Grashof number. The figure shows that only a small portion of the separating shear-layer is reattached to the stepped wall for the case where the Grashof number is 4000, while the rest of the region that is close to the step is vented directly to the main flow.

The effect of the Grashof number on the size of the reverse flow region that develops adjacent to the sidewall is shown Figs. 3 and 4. Results in Fig. 3 represent the linked points (a line) that identify the locations where the streamwise velocity component ($u$) is zero on a plane that is near the sidewall ($z/L=0.01$). Each one of the lines represents the downstream and the upstream boundaries of the reverse flow region that develops adjacent to the sidewall. At the downstream boundary the flow reverses its direction and starts flowing upstream toward the step, and at the upstream boundary that flow reverses its direction again to move in the downstream direction with the main flow. For low Grashof number, Gr<700, the reverse flow region adjacent to the sidewall develops at the upper corner of the sidewall and that region is separated from the primary recirculation flow region. As the Grashof number increases, Gr>700, the reverse flow region that develops adjacent to the sidewall merges with the primary recirculation flow region as shown in Fig. 3. These results also demonstrate that the primary recirculation flow region is vented to the main flow at the plane of $z/L=0.01$ for Grashof number equals to 4000, but the reverse flow region adjacent to the sidewall remains connected with the primary recirculation flow region at that plane. Results in Fig. 4 represent the linked points (a line) that identify the locations where the streamwise $u$-velocity component is zero on a plane near the flat wall of the duct at $y/S=1.99$. Each one of these lines represents the downstream and the upstream boundaries of the reverse flow region that develops adjacent to that wall, similar to what was described in Fig. 3. The depth of that region in the spanwise direction extends to approximately 15 percent of the duct's half width at Gr=0, but extends to approximately 40 percent of the duct's half width at Gr=4000.

Due to space limitations, graphical results for the effects of the Grashof number on velocity distributions are not presented in this Note. Results for the streamwise $u$-velocity component indicate that a "jet like" flow develops in the separating shear layer near the sidewall and the magnitude of the peak velocity decreases and moves closer to the sidewall with increasing Grashof number. Results for the transverse $v$-velocity component indicate that its magnitude is mostly negative due to sudden expansion in geometry with its peak increasing in absolute value as the Grashof number increases, and that peak develops at approximately the same height as the step. In the neighborhood of the sidewall, however, that trend is reversed and the magnitude of that velocity component decreases in absolute value and becomes positive as the Grashof number increases due to the reverse flow that develops in that region. A "jet like" flow develops in the spanwise distribution of that velocity component near the sidewall, and the magnitude of the peak in these distributions increases with increasing Grashof numbers. Results for the spanwise $w$-velocity component indicate that the flow is moving mostly from the wall toward the center of the duct, but in the corner near the sidewall and the stepped wall, the flow moves toward the sidewall to support the reverse flow that develops in that region. That reverse flow region increases in size as the Grashof number increases.

Distributions of Nusselt number ($\mathrm{Nu}=q_w S/k(T_w-T_0)$, where $T_w$ is the wall temperature and $T_0$ is the inlet fluid temperature) on the heated stepped wall are presented in Fig. 5 for different Grashof numbers. The maximum that occurs near the sidewall can be clearly seen in that figure. The development of this peak in the Nusselt number distribution near the sidewall is due to the "jet like" flow that develops in that region. The peak Nusselt number

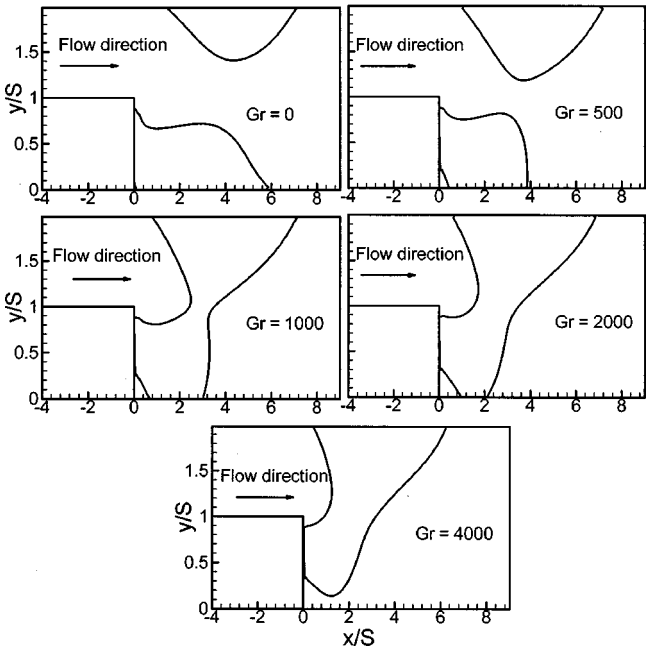


**Fig. 3 Effects of Grashof number on size of reverse flow region at a plane $z/L=0.01$**

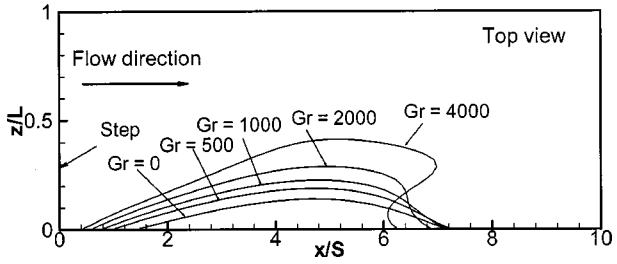


**Fig. 4 Effects of Grashof number on size of reverse flow region at a plane $y/S=1.99$**

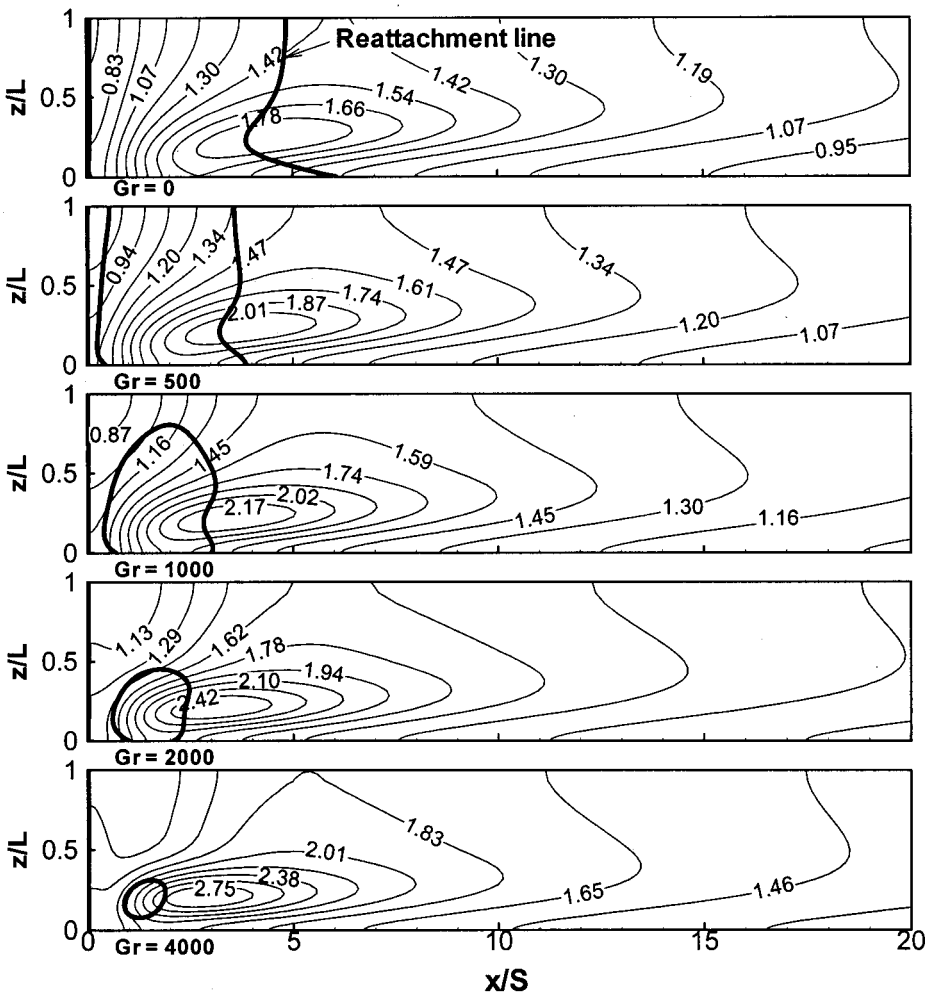


**Fig. 5 Effects of Grashof number on the Nusselt number distribution**

occurs in the same general region where the reattachment length is minimum, and it is downstream from the reattachment line. Reattachment lines are included in this figure for comparisons of relative positions. The maximum in that distribution moves upstream toward the step and closer to the sidewall as the Grashof number increases. The maximum Nusselt number increases from 1.85 at Gr=0, to 2.8 at Gr=4000.

## Conclusions

Numerical simulations of three-dimensional laminar buoyancy-assisting mixed convection flow adjacent to a backward-facing step in a duct are presented to demonstrate the influence of the Grashof number on the distributions of the Nusselt number, and the reverse flow regions that develop adjacent to the duct's walls in this geometry. Increasing the Grashof number results in increasing the Nusselt number; the size of the secondary recirculation flow region adjacent to the stepped wall; the size of the reverse flow region adjacent to the sidewall and the flat wall; and the spanwise flow from the sidewall toward the center of the duct. On the other hand, the size of the primary recirculation flow region adjacent to the stepped wall decreases and detaches partially from the heated stepped wall as Grashof number increases. The locations of the maximum Nusselt number move upstream toward the step and closer to the sidewall as the Grashof number increases. The ''jet like'' flow that develops near the sidewall is responsible for developing a minimum in the spanwise distributions of the reattachment length and a maximum in the spanwise distributions of Nusselt number near the sidewall. The reverse flow region that develops adjacent to the sidewall is not connected to the primary recirculating flow region for the cases of low Grashof number (Gr=0.0, and 500) but becomes connected to that region at higher Grashof numbers.

## Acknowledgments

This work was supported in part by the National Science Foundation (NSF) under grants No. CTS-9906746, and CTS-9818203.

## References

[1] Armaly, B. F., Durst, F., Pereira, J. C. F., and Schonung, B., 1983, ''Experimental and Theoretical Investigation of Backward-Facing Step Flow,'' J. Fluid Mech., **127**, pp. 473–496.
[2] Simpson, R. L., 1996, ''Aspects of Turbulent Boundary-Layer Separation,'' Prog. Aerosp. Sci., **32**, pp. 457–521.
[3] Eaton, J. K., and Johnson, J. P., 1981 ''A Review of Research on Subsonic Turbulent Flow Reattachment,'' AIAA J., **19**, pp. 1093–1100.
[4] Iwai, H., Nakabe, K., and Suzuki, K., 1999, ''Numerical Simulation of Buoyancy-Assisting, Backward-Facing Step Flow and Heat Transfer in a Rectangular Duct,'' Journal of Heat Transfer—Asian Research, **28**, pp. 58–76.
[5] Pepper, D. W., and Carrington, D. B., 1997, ''Convective Heat Transfer Over a 3-D Backward Facing Step,'' *Proceedings of the ICHMT Int. Symp. on Advances in Computational Heat Transfer*, G. de Vahl Davis and E. Leonardi, eds., pp. 273–281.

[6] Armaly, B. F., Li, A., and Nie, J. H., 2001, ''Three-Dimensional Laminar Forced Convection Adjacent to a Backward-Facing Step,'' J. Thermophys. Heat Transfer, in press.
[7] Iwai, H., Nakabe, K., and Suzuki, K., 2000, ''Flow and Heat Transfer Characteristics of Backward-Facing Step Laminar Flow in a Rectangular Duct,'' Int. J. Heat Mass Transf., **43**, pp. 457–471.
[8] Iwai, H., Nakabe, K., Suzuki, K., and Matsubara, K., 2000, ''The Effects of Duct Inclination Angle on Laminar Mixed Convective Flows Over a Backward-Facing Step'' Int. J. Heat Mass Transf., **43**, pp. 473–485.
[9] Li, A., and Armaly, B. F., 2000, ''Mixed Convection Adjacent to 3-D Backward-Facing Step,'' *Proceedings of the ASME-IMECE Conference*, ASME HTD, 366-2, pp. 51–58.